



## Research Article

# The HI in Ring Galaxies Survey (HI-RINGS)—Effects of the bar on the HI gas in ring galaxies

C. Murugeshan<sup>1</sup>, R. Džudžar<sup>2,3</sup>, R. Bagge<sup>4,5</sup>, T. O’Beirne<sup>5,1</sup>, O. I. Wong<sup>1,5</sup>, V. A. Kilborn<sup>2,6</sup>, M. E. Cluver<sup>2,7</sup>,  
K. A. Lutz<sup>8</sup> and A. Elagali<sup>9,10</sup>

<sup>1</sup>ATNF, CSIRO, Space and Astronomy, PO Box 1130, Bentley, WA 6102, Australia, <sup>2</sup>Centre for Astrophysics and Supercomputing, Swinburne University of Technology, Hawthorn, VIC 3122, Australia, <sup>3</sup>Tribalium PTY LTD, Lvl 1, 25 King Street, Melbourne, VIC 3000, Australia, <sup>4</sup>School of Physics, The University of New South Wales, Kensington Campus, Old Main Building, Kensington, Sydney, NSW, Australia, <sup>5</sup>International Centre for Radio Astronomy Research, The University of Western Australia, 35 Stirling Highway, Crawley, WA 6009, Australia, <sup>6</sup>ARC Centre of Excellence for All Sky Astrophysics in 3 Dimensions (ASTRO 3D), Australia, <sup>7</sup>Department of Physics and Astronomy, University of the Western Cape, Robert Sobukwe Road, Bellville, 7535, South Africa, <sup>8</sup>Observatoire Astronomique de Strasbourg, Université de Strasbourg, CNRS, UMR 7550, 67000 Strasbourg, France, <sup>9</sup>Minderoo Foundation, 171 - 173 Mounts Bay Road, Perth, WA 6000, Australia and <sup>10</sup>School of Biological Sciences, The University of Western Australia, 35 Stirling Highway, Crawley, WA 6009, Australia

### Abstract

We present a new high-resolution neutral atomic hydrogen (HI) survey of ring galaxies using the Australia Telescope Compact Array (ATCA). We target a sample of 24 ring galaxies from the Buta (1995) Southern Ring Galaxy Survey Catalogue in order to study the origin of resonance-, collisional- and interaction-driven ring galaxies. In this work, we present an overview of the sample and study their global and resolved HI properties. In addition, we also probe their star formation properties by measuring their star formation rates (SFR) and their resolved SFR surface density profiles. We find that a majority of the barred galaxies in our sample are HI-deficient, alluding to the effects of the bar in driving their HI deficiency. Furthermore, for the secularly evolving barred ring galaxies in our sample, we apply Lindblad’s resonance theory to predict the location of the resonance rings and find very good agreement between predictions and observations. We identify rings of HI gas and/or star formation co-located at one or the other major resonances. Lastly, we measure the bar pattern speed ( $\Omega_{\text{bar}}$ ) for a sub-sample of our galaxies and find that the values range from 10–90 km s<sup>−1</sup>kpc<sup>−1</sup>, in good agreement with previous studies.

**Keywords:** galaxies: evolution – galaxies: fundamental parameters – galaxies: ISM – galaxies: kinematics and dynamics

(Received 31 October 2022; revised 28 March 2023; accepted 30 March 2023)

### 1. Introduction

Galaxies come in a variety of shapes and sizes and have been traditionally classified on the basis of their optical morphology (e.g., Hubble 1926; de Vaucouleurs 1959). Hubble developed the famous ‘tuning-fork’ diagram which sorted galaxies broadly into spheroidal/elliptical early-type galaxies towards one end of the fork, gradually transitioning into more and more late-type disk galaxies, which are observed to possess features such as a nucleus, bar and spiral arms to name a few. Galaxies were further classified on the basis of how tightly wound their spiral arms were and on the presence or absence of a bar, forming the two prongs in the tuning fork diagram. Apart from the early- and late-type galaxies, Hubble also identified galaxies that did not specifically fit into one or the other group and classified them as peculiar galaxies. In the following decades a number of atlases of galaxies were curated in an attempt to uniformly classify galaxies, one of the most important ones being the atlas compiled by Sandage (1961), who expanded on the existing Hubble classification scheme and introduced a special class of galaxies called ring galaxies. Such

galaxies were observed to possess ring-like structures based on their optical images. This classification scheme was further revised by de Vaucouleurs et al. (1991), who introduced a number of sub-classes of ring galaxies, including those galaxies having nuclear, inner and outer (pseudo-) rings and lenses.

Depending on the morphology of the ring, its position, alignment and size, ring galaxies are typically classified into the following major types: Resonance rings, collisional, accretion and polar rings (for a full review see Buta & Combes 1996). While the exact mechanisms driving the formation of rings in galaxies are still debated, the following are believed to be some of the major scenarios:

**1. Resonance rings driven by the bar:** Stars and gas orbiting the inner parts of a galaxy possessing a bar respond to the torques exerted by the non-axisymmetric potential of the bar and settle into orbits of resonance (Lindblad 1964; Schwarz 1981). In addition to the accumulation of stars and gas from the disk, due to the increased density and pressure at these resonance locations, the gas collapses to form new stars, resulting in the formation of stellar ring-like structures that is visible in the UV, optical and infrared (IR) bands (Buta & Combes 1996; Buta, Byrd, & Freeman 2004; Grouchy et al. 2010 and references therein). Numerous sub-classes exist within resonance rings, such as nuclear rings, inner (pseudo) rings and outer (pseudo) rings (e.g., Comerón et al. 2014). Outer

**Corresponding author:** C. Murugeshan, Email: [chandrashekar.murugeshan@csiro.au](mailto:chandrashekar.murugeshan@csiro.au).  
**Cite this article:** Murugeshan C, Džudžar R, Bagge R, O’Beirne T, Wong OI, Kilborn VA, Cluver ME, Lutz KA and Elagali A. (2023) The HI in Ring Galaxies Survey (HI-RINGS)—Effects of the bar on the HI gas in ring galaxies. *Publications of the Astronomical Society of Australia* 40, e018, 1–28. <https://doi.org/10.1017/pasa.2023.19>

pseudo rings are observed to be formed by two tightly wound spiral arms in late-type galaxies that almost form a complete ring in the outskirts of galaxies (Buta 1993). Pseudo rings are purported to be reflective of an earlier stage in ring formation in galaxies, as they are more common in late-type galaxies, while complete rings are more common among early-type disk galaxies (Elmegreen *et al.* 1992; Buta 1993; Buta & Combes 1996). The theoretical models of Schwarz (1981) however predict both rings and pseudo rings to occur close to the Lindblad resonance radii in galaxies. We present a more detailed discussion of resonance rings in Section 4.

**2. Driven by galaxy-galaxy collisions:** Simulations have shown that galaxy collisions could lead to the formation of ring galaxies (Appleton *et al.* 1996; Wong *et al.* 2006; Elagali *et al.* 2018 and references therein). In a drop-through collision, typically a smaller ‘bullet’ galaxy passes through the (off-)centre of a larger disk galaxy, sending out shock waves that push both the stellar and gas material outward to form a ring-like structure. Many such systems have thus far been observed including the famous Cartwheel galaxy AM 2026-424 (Zwicky 1941), and the recently discovered high-redshift collisional ring galaxy R5519 (Yuan *et al.* 2020).

**3. Driven by accretion of gas from the IGM:** In few ring systems such as Hoag’s galaxy (Hoag 1950), the Leo ring (Schneider *et al.* 1983), AGC 203001 (Bait *et al.* 2020), the formation of the ring structure is attributed to the accretion of fresh gas from the surrounding IGM onto a ring, under favourable conditions (Lynds & Toomre 1976; Theys & Spiegel 1977; Schweizer *et al.* 1987). Star formation starts as soon as the accreted HI gas column density exceeds a threshold. In some cases, for example the Leo ring and AGC 203001 (Bait *et al.* 2020), the accreted HI gas column density is low enough that significant star formation does not occur, leaving only an HI ring behind with no stellar counterpart. Polar rings are another class of ring galaxies which are believed to have accreted HI gas, but that gas has settled into polar orbits around the galaxy. Typically, polar ring galaxies are observed to be S0-type galaxies which have recently accreted fresh HI gas from either a smaller companion dwarf galaxy or directly from the IGM. To date over 400 potential polar ring galaxy candidates have been identified, but only a dozen or more galaxies have been confirmed to be polar rings (Moiseev *et al.* 2011; Egorov & Moiseev 2019; Nishimura *et al.* 2022). As such, polar ring galaxies are a rare class of ring galaxies.

Ring galaxies have been studied extensively in the optical, UV, NIR and FIR bands. Early photometric studies revealed that the location of the rings were hot-spots for active star formation, which was determined from their distinct patchy blue distribution (Sandage 1961; Athanassoula & Bosma 1985). Buta & Combes (1996) find that among the catalogue of bright nearby galaxies, outer (pseudo)rings are found only for about 10% of the sample. Buta (1995) compiled a comprehensive list of 3692 ring galaxies, with the objective of studying if the rings in galaxies were linked to orbital resonances. They speculate that the observed outer (pseudo)rings may be associated with the outer Lindblad resonance, while the inner rings are associated with the Ultra-harmonic resonances. They suggest that measuring the location of the inner and outer rings may be useful to indirectly measure the bar pattern speed. For a full review of the various studies

undertaken in the different wavelength regimes we refer the reader to Buta & Combes (1996).

In terms of the HI gas in ring galaxies, most studies have focused on the unresolved, global HI gas properties with a handful of high-resolution HI studies limited to small samples. One of the first high-resolution study of the HI gas distribution in a ring galaxy was undertaken by Bosma, van der Hulst, & Sullivan (1977) for the spiral galaxy NGC 4736, via synthesis imaging using the Westerbork Radio Synthesis Telescope (WSRT). They find that the HI gas in this galaxy is observed to trace not only the optically bright central regions, but also the faint outer stellar ring. Following this, a few targeted HI studies focusing on a few galaxies were conducted, most of which revealed HI rings to be roughly co-located with the outer stellar rings (see for example Knapp *et al.* 1984; van Driel, Rots, & van Woerden 1988; van Driel & Buta 1991). Some early HI studies have also identified galaxies for which rings of HI gas are found with no obvious optical ring-like structures (see for example Krumm, van Driel, & van Woerden 1985; Tilanus & Allen 1993). Overall, such studies have hinted at the importance of the HI gas in forming the ring-like stellar structures observed in galaxies.

Apart from a few targeted HI studies, to date, there is no large comprehensive study of the resolved HI gas distribution and kinematics of ring galaxies. HI gas is an excellent tracer of both internal and external processes affecting galactic evolution. In addition, HI gas is the fundamental source of molecular hydrogen ( $H_2$ ), which is eventually converted to stars in low- $z$  galaxies (Meurer *et al.* 2006). This link proves even more useful in the context of tracing star formation in the different types of ring galaxies. Therefore, such a study will be an important step towards understanding how the HI gas in these systems is distributed and also enable us to study the effects of the environment on such systems. This may be particularly useful in the context of understanding ring formation in galaxies linked to tidal interactions and external perturbations (e.g., Combes *et al.* 1990). In addition, from the gas kinematics we can measure the angular momentum (AM) in the ring and examine the link between gas stability and the role of AM in regulating star formation in the ring. HI studies of ring galaxies are therefore very important to understand both the morphology and kinematics of the rings, allowing us to understand the various processes (both internal and environmental) driving their formation.

It is important to distinguish mechanisms that lead to the formation of ring galaxies (visible in their optical and HI morphology) as discussed above compared to HI ‘holes’ and HI ‘depressions’ at the centres of galaxies that may be linked to the natural process of star formation where the HI gas is converted to and eventually stars (see Walter *et al.* 2008; Leroy *et al.* 2008; Murugesan *et al.* 2019) and do not necessarily coincide with the optical rings. In this paper, we introduce a sample of ring galaxies which have been identified through their optical morphology to possess ring-like structures (see Section 2.1 for more details on the selection criteria). We probe the distribution of the HI gas in such systems and study their kinematics. In the next sub-section we introduce this new survey of ring galaxies.

### 1.1. The HI in Ring Galaxies Survey (HI-RINGS)

In order to address the diversity of ring galaxy evolution in terms of the gas kinematics, we have put together a new high-resolution

HI survey of ring galaxies—the HI in Ring Galaxies Survey (HI-RINGS), targeting different types of ring galaxies, to study their HI and star formation properties using a uniform and large sample of 24 galaxies. We have procured new Australia Telescope Compact Array (ATCA) observations for 15 ring galaxies in addition to compiling ATCA data from the archive for 9 galaxies. Our sample consists of various types of ring galaxies including resonance, collisional and interaction rings, enabling us to probe their HI gas distribution, resolved star formation and star formation rate (SFR) surface densities, as well as their kinematic properties, using a multiwavelength approach including optical and infrared data.

Through this paper and the following series of papers, we hope to address important questions pertaining to the formation and evolution of ring galaxies in the local Universe. Below we list some of the main goals of the HI-RINGS survey.

- Test Lindblad’s resonance theory using robust rotation curves for a large sample of ring galaxies. We will utilise the rotation curves to derive the bar pattern speeds and predict the location of the resonance rings. In addition, we aim to study the HI gas and SFR surface densities to probe the nature of the distribution of both gas and star formation in our sample galaxies.
- We aim explore the HI/H<sub>2</sub> ratio in ring galaxies. It has been observed in several collisional ring galaxies that the HI/H<sub>2</sub> ratio is large, this could mean that in such galaxies the H<sub>2</sub> is being efficiently converted into stars (Higdon, Higdon, & Rand 2011; Wong et al. 2017). We intend to compare the HI/H<sub>2</sub> ratio among the different types of ring galaxies in our sample to understand the HI to H<sub>2</sub> conversion phase in such systems. More than half the galaxies in our sample have high-resolution ALMA observations of CO. By complementing this with high-resolution HI data, we will be able to study the HI/H<sub>2</sub> ratios for a large sample of spatially resolved ring galaxies.
- Obreschkow et al. (2016) introduced the  $f_{\text{atm}} - q$  relation, where  $f_{\text{atm}}$  is the neutral atomic gas fraction and  $q \propto j_{\text{b}}/M_{\text{b}}$  is the integrated disk stability parameter, where  $M_{\text{b}}$  is the total baryonic mass and  $j_{\text{b}}$  is the total specific baryonic angular momentum (sAM) of the galaxy. Both HI-excess and HI-deficient late-type galaxies have been found to follow this relation consistently (Lutz et al. 2017, 2018; Murugesan et al. 2019), indicating that sAM plays a fundamental role in regulating the HI gas content in galaxies. Murugesan et al. (2019) find two ring galaxies in their sample that follow the  $f_{\text{atm}} - q$  relation. However, do all galaxies possessing rings that are in gravitational equilibrium follow the  $f_{\text{atm}} - q$  relation? We will use the high-resolution HI data to accurately model the kinematics of ring galaxies, measure their sAM and study their behaviour on the  $f_{\text{atm}} - q$  plane. Such a study will give us important clues about the role of angular momentum in regulating the stability of the HI gas in the ring.
- What is the effect of the local and global environment on the formation of ring galaxies? Elagali et al. (2018) found that 83% of ring galaxies in the EAGLE simulations were formed via a ‘drop-through’ collision. Our sample of ring galaxies spans across a range of local density environments, being associated with the field, group or cluster.

With our sample of ring galaxies, we aim to study how the environment affects the properties of ring galaxies.

In this work, we introduce the HI-RINGS survey and give an overview of the sample. We model the HI kinematics for the sample galaxies using 3D tilted-ring fitting and derive robust rotation curves. Using the rotation curves we accurately derive the bar pattern speed for the barred galaxies in our sample and test Lindblad’s theory of ring formation. In addition, we also explore the effects of the bar on the resolved and global HI and star formation properties of galaxies. We structure the paper as follows—in Section 2 we give details on the sample selection, observations, data reduction, source finding and 3D modelling. Following this, in Section 3 we present the main results, including an overview of the sample and their measured properties. In Section 4, we test resonance theory of ring formation based on the analysis of a sub-sample of barred galaxies in our sample. Finally, in Section 5, we summarise the main results and give an outline of the plans for the future.

## 2. Data and methods

In this section we will discuss the criteria applied for the sample selection, give details of the observations, list the steps followed in the data reduction process and discuss the source finding and characterisation. We will also describe the kinematic modelling for the sample galaxies which is necessary to derive their rotation curves.

### 2.1. Sample selection

We use the Catalogue of Southern Ringed Galaxies (CSRG, Buta 2001), obtained through the Vizier catalogue access tool (Ochsenbein, Bauer, & Marcout 2000) to select our sample of ring galaxies. The CSRG was originally published by Buta (1995), presenting properties of outer and inner rings, pseudo-rings and lenses of 3692 galaxies south of  $-17^\circ$  in declination.

Our selection criteria was based on galaxy size, position, visual inspection of each galaxy from CSRG, and a cross-check as to whether the galaxies were detected in the HI All Sky Survey (HIPASS, Barnes et al. 2001; Meyer et al. 2004):

- Our primary selection criteria was galaxy size, selecting galaxies with large angular size, sufficient to resolve the HI in the rings, to be able create reliable kinematic models. We selected galaxies with  $D_{25} \geq 180''$ , where  $D_{25}$  is the B-band 25 mag arcsec<sup>-2</sup> isophotal diameter, from ESO-LV ‘Quick Blue’ IIa-O (Lauberts & Valentijn 1989).
- The secondary constraint was declination of the galaxy, selecting galaxies south of  $-25^\circ$  in declination. This criteria ensures good observability with the ATCA, avoiding an elongated synthesised beam.
- Using Astroquery SkyView cutout service (Ginsburg et al. 2019), we obtained DSS images of all  $\sim 3692$  galaxies from the CSRG and visually inspected them. This step was necessary to validate the galaxy selection process and it was done before and after size/declination restrictions to the catalogue. Next, with visual inspection of 101 ring galaxies—obtained after the declination and size restrictions—we removed highly edge-on galaxies and galaxies with no clear rings and/or inner (pseudo)rings.



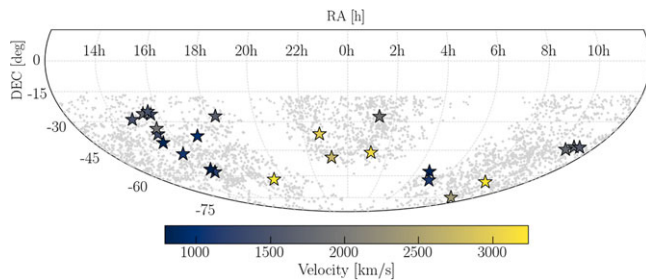


**Figure 1.** Spatial and velocity distribution of galaxies in the HI in Ring Galaxies Survey (HI-RINGS). The grey points show all the ring galaxies from the (Buta 1995) catalogue, the stars show our sample of ring galaxies where colour denotes their Heliocentric velocity.

Galaxies with unclear/faint images were re-checked in NED database. Additionally, two ring galaxies—ESO 215-31 and ESO 179-IG-013, were added to our sample through visual inspection.

- As a final check, we inspected the HIPASS data to see if the selected galaxies have an HI detection. This step was necessary to minimise risk of not detecting HI through our new ATCA observations. With this check five galaxies were removed due to HI non-detection in HIPASS.

The above criteria left us with a sample of 27 ring galaxies of the  $\sim 3692$  from the original CSRG sample, as the majority of galaxies have an angular size too small to be sufficiently resolved with the ATCA. Out of the 27, 12 galaxies were found to have archival ATCA data (in the 1.5 km, 750 m and 352/375 m configurations). We have observed 15 ring galaxies with our ATCA proposal (C3385). Ultimately, due to calibration issues and/or not being able to derive reliable kinematic models, 3 of the 12 galaxies from the archive were rejected, leaving us with a final sample size of 24 ring galaxies. Figure 1 shows the spatial and velocity distribution of our sample of ring galaxies.

## 2.2. Observations

The 15 galaxies in our sample, for which no archival data are available, were observed with the ATCA in one of the default 750 m and 1.5 km array configurations. These observations were carried out through the ATCA project C3385 in 2020OCTS and 2021APRS semesters with a total observation time of 307.5 h, and an average on-source time of  $\sim 11$  h per array configuration. Combining the data from these two configurations will result in increasing both sensitivity and spatial resolution of the synthesised data, which is key to accurately modelling the kinematics of the sample galaxies (see Section 2.7). The ATCA, which is equipped with the Compact Array Broad-band Backend (CABB, Wilson *et al.* 2011), allows us to observe the galaxies in both continuum and spectral-line mode. The total bandwidth in the continuum band is 2048 MHz with a frequency resolution of 1 MHz, centred at 2.1 GHz. The spectral line observations have a total bandwidth of 8.5 MHz with a channel resolution of 0.5 kHz, which corresponds to a velocity resolution of  $\sim 1$  km s $^{-1}$ . We employed the following strategy for the observations—55 min on source followed by 5 min on the phase calibrator each hour. The primary calibrators used are PKS 1934-638 and PKS 0823-500 depending on the time of observations. The primary calibrator was observed for 10 min at the start and end of the observing run. Other details of the observations for the sample are listed in Table 1.

## 2.3. Archival ATCA data

As mentioned previously, 9 galaxies in our sample have archival ATCA data in both the standard 1.5 km and 750 m array configurations. The data was retrieved from the Australia Telescope Online Archive (ATOA). For a few galaxies we also found observations in the 350 m array configuration. The exact configurations used for the data reduction for the various galaxies in our sample is listed in Table 1.

## 2.4. Data reduction

We used the MIRIAD software package (Sault, Teuben, & Wright 1995) to reduce the ATCA data. The 750 m and 1.5 km array data (and for some galaxies the 375 and 352 m data) were reduced separately and later combined to produce the final visibility data set. The following steps are carried out in the data reduction process—first we flag any spurious data using UVFLAG and PGFLAG. Once the quality of the data looks good, we then perform the bandpass and phase calibration using the tasks MFCAL, MFBOOT, GPCAL and GPBOOT. This is then followed by continuum subtraction using UVLIN. We iteratively select line-free channels in the data for the continuum subtraction process. Following this, we use the INVERT task to Fourier transform the UV data to form a dirty image. The visibility data from the 1.5 km and 750 m configurations are combined using the INVERT task after continuum subtraction has been carried out on the individual data sets. The INVERT task also estimates the expected theoretical rms noise in the image cube. We use the  $3\sigma$  value of this estimate as cutoff during the ‘cleaning’ process. Next, we proceed to the de-convolution step, which is performed using the CLEAN algorithm in MIRIAD. We set the number of iterations for the minor CLEAN cycle to 2000 and wait for CLEAN to reach the cutoff value. Following the de-convolution step, we restore the final image cube using the RESTOR task. Finally, we apply the primary beam correction to the restored image cube using the LINMOS task.

We set the robustness parameter to 0.5, as it offers a good compromise between sensitivity and resolution. The semi-major axis values of the synthesised beam (BMAJ) range from 31 to 93 arcsec, with a median beam size of  $\sim 40$  arcsec. The channels were also smoothed to a width of 5 km s $^{-1}$ , thereby increasing the signal-to-noise-ratio (SNR) in the image cubes. The median  $3\sigma$  rms noise level in the image cubes for our galaxy sample is  $\sim 4.92$  mJy beam $^{-1}$  per channel, which corresponds to a column density sensitivity limit of  $N_{\text{HI}} \sim 1.7 \times 10^{19}$  cm $^{-2}$  assuming an observed median beam size of  $\sim 40$  arcsec.

## 2.5. Source finding with SoFiA

We make use of the Source Finding Application (SoFiA; Serra *et al.* 2015; Westmeier *et al.* 2021) to automatically detect sources in the final image cubes. We have used the smooth + clip (S + C) algorithm in SoFiA to build the source mask. The S + C finder works by spatially and spectrally smoothing the data cube on multiple scales as defined by the user. In each smoothing iteration, a user-specified flux threshold relative to the global rms noise level after smoothing is applied to the data, and all pixels with an absolute flux density exceeding that threshold is used to create the source mask (Westmeier *et al.* 2021). The multi-scale smoothing and clipping helps in identifying relatively faint and extended features in the data cubes that may have been missed otherwise. After the source finding run, SoFiA returns a number of

**Table 1.** Details of the observations. Col (1): Common name; (2) ATCA baseline observation configuration; Col (3): The central frequency of the observation; Col (4): Primary flux calibrator used; Col (5): Phase calibrator used; Col (6): rms in the image cubes; Col (7): Synthesised beam size major and minor axis, respectively; Col (8): Notes about observations: This survey—ATCA project C3385; NGC 1433 data is from C305 (Ryder et al. 1996); NGC 7531 data is from C2196 (Koribalski et al. 2009); NGC 1808 data is from C585 (Dahlem, Ehle, & Ryder 2001); NGC1533 data is from C934 and C1003 (Ryan-Weber, Webster, & Staveley-Smith 2003); NGC 7098 data is from C744 (Pisano, Wilcots, & Liu 2002).

Name	Array configurations	$\nu_0$ (MHz)	Primary calibrator	Secondary calibrator	rms (mJy beam <sup>-1</sup> )	Synthesised beam (arcsec)	Notes
(1)	(2)	(3)	(4)	(5)	(6)	(7)	(8)
ESO 215-31	750 m & 1.5 km	1407	1934-638	0823-500	0.67	43×30	This survey
ESO 269-57	750 m & 1.5 km	1405	1934-638 & 0823-500	1320-446	2.20	43×30	This survey
NGC 1326	750 m & 1.5 km	1413	1934-638	0332-403	1.06	93×25	This survey
NGC 3358	750 m & 1.5 km	1406.3	1934-638	1015-314	1.85	54×31	This survey
IC 5267	750 m & 1.5 km	1412.2	1934-638	2311-452	1.09	49×29	This survey
NGC 1302	750 m & 1.5 km	1412	1934-638	0237-233	1.53	73×28	This survey
NGC 1398	750 m & 1.5 km	1413	1934-638	0413-210	1.26	68×27	This survey
NGC 2217	750 m & 1.5 km	1412	1934-638	0614-349	2.13	74×30	This survey
NGC 7020	750 m & 1.5 km	1405.2	1934-638	2117-642	1.67	38×30	This survey
NGC 1291	750 m & 1.5 km	1416	1934-638	0332-403	1.62	48×29	This survey
NGC 1371	1.5 km	1413.2	1934-638	0413-210	2.58	50×19	This survey
ESO 179-IG-013	750 m & 1.5 km	1416	1934-638	1613-586	2.09	36×29	This survey
NGC 1079	1.5 km	1413.2	1934-638	0237-233	2.41	57×19	This survey
NGC 5101	1.5 km	1411.7	1934-638	1308-220	2.71	54×19	This survey
IC 5240	750 m & 1.5 km	1411.7	1934-638	2226-411	0.99	48×28	This survey
NGC 1350	750 m & 1.5 km	1415.5	1934-638	0237-233	0.94	57×23	Murugesan et al. (2019)
NGC 2369	750 m & 1.5 km	1409	0823-500	0637-752	2.33	31×24	Murugesan et al. (2019)
NGC 7098	375 m & 750 m	1410	1934-638	2142-758	4.09	74×58	C744
NGC 1543	750 m & 1.5 km	1419	1934-638	0420-625	1.25	37×29	Murugesan et al. (2019)
NGC 1533	375 m, 750 m & 1.5 km	1417	1934-638	0407-658	8.2	35×27	C934 and C1003
NGC 1808	750 m & 1.5 km	1414	1934-638	0521-365	1.00	50×30	C585
NGC 7531	352 m & 1.5 km	1412.8	1934-638	2311-452	3.29	91×62	C2196
NGC 1433	750 m & 1.5 km	1415	0438-436	0438-436	1.32	46×34	C305
NGC 6300	750 m & 1.5 km	1415	1934-638	1718-649	0.96	36×22	Murugesan et al. (2019)

data products including a catalogue with source-specific parameters such as their RA, Dec, systemic velocity ( $V_{\text{sys}}$ ), integrated flux ( $S_{\text{int}}$ ),  $w_{20}$  and  $w_{50}$  velocity widths and kinematic position angle (P.A) based on the HI gas kinematics. In addition, SoFiA also produces cutouts of the spectral cube, moment 0 (intensity), moment 1 (velocity) and moment 2 (dispersion) maps for all detected sources from the inputted image cube. We make use of the spectral cubes and moment maps derived from SoFiA for the rest of our analysis.

## 2.6. Interactive visualisation of the HI-RINGS galaxies

Using Streamlit, an open-source Python library, we have built a web application for interactive visualisation of our HI-RINGS survey.<sup>a</sup> The web application allows the user to interactively explore our sample of ring galaxies using HI intensity data together with data from several other surveys including the DSS, WISE, 2MASS and GALEX. Within the app, it is possible to overlay selected HI contours on top of image cutouts from the different

surveys. The app also allows image comparison with and without HI contours, and image comparison with different survey images in the background. We believe such an interactive tool will be both informative as well as provide important visual context into the distribution of the HI and stellar components of the different types of ring galaxies in our sample. We provide further details on the web application in Appendix A. In addition, we plan to release the reduced HI data products for the HI-RINGS sample.

## 2.7. Tilted ring modelling with 3DBarolo

We perform 3D tilted-ring fitting (Rogstad, Lockhart, & Wright 1974) to the HI emission observed in the data cubes for our sample galaxies using the publicly available software 3DBarolo (Di Teodoro & Fraternali 2015). 3DBarolo takes in a user-specified parameter file containing initial guesses for the fitting and outputs the best fit tilted-ring model for the galaxy. For the fitting strategy we follow the steps described in Murugesan et al. (2019). 3DBarolo fits  $n$  independent tilted rings (where  $n$  is the total number of resolution elements across the major axis) of width equivalent to half the FWHM of the resolution element (which varies

<sup>a</sup>Link to the interactive web app: <https://hi-rings.streamlitapp.com/>.

from galaxy to galaxy in our sample). The fitting is performed in two stages—in the first stage the user-defined initial guesses for the galaxy centre (set to the optical/NIR centres obtained from NED<sup>b</sup>), the systemic velocity ( $V_{\text{sys}}$ ) and position angle (PA) are set to the values determined from the SoFiA source finding run. The initial guess for the inclination angle ( $i$ ) is set to the value determined by Lauberts & Valentijn (1989) based on the  $B$ -band optical surface photometry of the galaxies. We allow PA,  $i$  and the rotation velocity ( $v_{\text{rot}}$ ) to vary as free parameters during the fit. Once the best fitting model is derived from the first stage, the code uses these values in the second stage of the fitting. Finally, the best fitting values for PA,  $i$  and  $v_{\text{rot}}$  for every ring is written-out to a log file. The best fit model parameters such as  $v_{\text{rot}}$ ,  $i$  and PA are shown for the full sample in Figures B.10 and B.11 in Appendix B.

We do note that since we are dealing with ring galaxies and deriving their rotation curves from resolved HI observations, there is the danger of missing the HI signal from the very centres of these galaxies (assuming the HI gas is primarily co-located with the optical ring). Upon investigation, we find that this is not the case for the majority of our sample galaxies. We find that in most cases there is still HI emission from their centres and that the SNR of the HI emission is high enough for 3DBarolo to accurately fit the rotation curve in the inner regions. We find four galaxies in our sample, namely, NGC 1326, NGC 1371, NGC 5101 and NGC 1534, for which the SNR of the HI emission at the centre is too low for 3DBarolo to effectively create a source mask and fit a kinematic model. We note that this might potentially affect the resonance analysis we perform in Section 4 for the above galaxies. This is because the prediction of the resonance locations are dependent on their rotation curves. That being said, since the location of the resonance rings are mainly dependent on the outer parts of the rotation curve, we believe this should not significantly affect our analysis.

### 3. Results

We now discuss some general properties of the ring galaxies in our sample as well as present the main results.

#### 3.1. Flux comparison with HIPASS

As described in Section 2.5, we use SoFiA to automatically detect the sources in the image cubes and also obtain a catalogue consisting of relevant HI parameters including the integrated flux. We check the quality of the data and as a validation step compare the integrated flux derived from the SoFiA run for our sample galaxies with their HIPASS flux values. Figure 2 shows a plot comparing the integrated flux from the ATCA observations with their corresponding HIPASS fluxes. For the majority of the sources, we find a good one-to-one correspondence. About 7 galaxies in our sample ( $\sim 29\%$ ) are observed to have a low integrated flux compared to their HIPASS flux. We attribute this to a combination of two effects: (1) Missing diffuse flux—Three galaxies NGC 1371, NGC 1079 and NGC 5101 only have observations in the 1.5 km array configuration. This means that these galaxies are very likely missing the extended diffuse emission that the shorter baselines may have otherwise captured. This is also evidenced by the fact that the HIPASS  $w_{20}$  values are typically  $\sim 9\%$  broader than the ATCA  $w_{20}$  values; (2) Confusion in the HIPASS flux—Galaxies

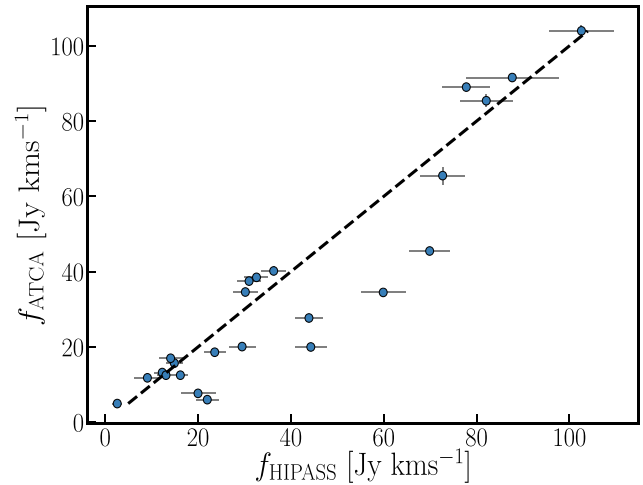


**Figure 2.** The plot compares the integrated flux for the ring sample derived from our ATCA observation (on the Y-axis) against their corresponding integrated flux from HIPASS (X-axis). The dashed black line represents the one-to-one correspondence.

NGC 1326 and NGC 3358 are observed to have close companions spatially and/or in velocity space. Owing to the larger  $\sim 15$  arcmin HIPASS beam, it is likely that the HIPASS flux is confused and overestimated for these two galaxies. This is also clearly seen in Figure B.12, where we compare their HIPASS and ATCA spectra. We examine the rms noise level in the image cubes and find them to be between  $0.67$ – $8.2$  mJy beam<sup>-1</sup> per channel. This is close to the expected theoretical noise given the integration time and UV-coverage of the individual observations. In the following sections we present the main results from our study.

#### 3.2. Sample overview and HI properties

In this section we give an overview of both the global and resolved properties of the ring galaxies in our sample. Figures B.1–B.4 in Appendix B show the optical images of the sample galaxies with the HI contours overlaid on top, as well as their HI velocity maps. From the optical images, we find that most of the galaxies in our sample are early late-type galaxies with their morphology ranging from (SA, SAB to S0). In addition to the presence of optical rings, we also notice the HI gas distributed in the form of rings, in many cases (almost) co-located with the optical rings (NGC 1326, NGC 1398, NGC 2217, IC 5240, NGC 1350, NGC 6300, ESO 215-31, NGC 1079, NGC 5101). We find this to be true typically for galaxies possessing bars in our sample. However, it is also interesting to note that the HI gas distribution in some ring galaxies is more complex. For example, galaxies ESO 215-31 and NGC 1808 are observed to have an excess of HI gas clumping at the ends of the bar and along the major axis of the bar, which may be indicative of gas inflows (see for example Salak *et al.* 2016 and references therein). From the velocity maps it is evident that most galaxies in our sample exhibit ordered rotational motion.

We make use of the Carnegie-Irvine Galaxy Survey (CGS; Ho *et al.* 2011) and the Third Reference Catalogue of Bright Galaxies (de Vaucouleurs *et al.* 1991) to confirm presence or absence of a bar for our sample galaxies. We visually observe that 14 galaxies in our sample have a strong bar, while the other 10 are observed to have a weak or no bar. For our analysis in the next sections, we therefore split the galaxies into two groups—those with a strong

<sup>b</sup><http://ned.ipac.caltech.edu/>.

**Table 2.** Ring galaxies derived sample properties. Col (1): Common name; Cols (2)–(3): Right Ascension and Declination in J2000; Col (4): Systemic velocity; Col (5): Distance; Col (6): Integrated flux derived from SoFIA; Cols (7)–(8): HI and stellar mass; Col (9): 5th nearest-neighbour density estimate; Col (10): Whether the galaxy has a strong, weak bar or does not have a bar. We refer to The Carnegie-Irvine Galaxy Survey (CGS; Ho et al. 2011) and the Third Reference Catalogue of Bright Galaxies (de Vaucouleurs et al. 1991) to confirm presence or absence of a bar.

Name	RA (J2000)	Dec (J2000)	$V_{\text{sys}}$ ( $\text{km s}^{-1}$ )	D (Mpc)	$S_{\text{int}}$ ( $\text{Jy km s}^{-1}$ )	$\log(M_{\text{HI}})$ ( $M_{\odot}$ )	$\log(M_{\star})$ ( $M_{\odot}$ )	$\Sigma_5$ ( $\text{Mpc}^{-2}$ )	Barred (10)
(1)	(2)	(3)	(4)	(5)	(6)	(7)	(8)	(9)	(10)
ESO215-31	11h10m34.79s	−49d06m09.4s	2722	35.20	$12.50 \pm 0.27$	$9.56 \pm 0.12$	$10.45 \pm 0.09$	0.05	Yes
ESO269-57	13h10m04.43s	−46d26m14.4s	3106	43.24	$38.5 \pm 0.81$	$10.19 \pm 0.10$	$10.79 \pm 0.10$	0.59	Yes
NGC1326	03h23m56.40s	−36d27m52.8s	1360	14.95	$7.67 \pm 0.26$	$8.61 \pm 0.11$	$10.32 \pm 0.08$	1.59	Yes
NGC3358	10h43m33.02s	−36d24m38.5s	2988	38.30	$6.00 \pm 0.33$	$9.32 \pm 0.15$	$10.80 \pm 0.07$	0.33	No
IC5267	22h57m13.57s	−43d23m46.1s	1712	21.26	$20.1 \pm 0.56$	$9.33 \pm 0.06$	$10.59 \pm 0.07$	0.18	No
NGC1302	03h19m51.18s	−26d03m37.6s	1710	11.21	$15.70 \pm 0.44$	$8.67 \pm 0.09$	$9.87 \pm 0.08$	0.32	Yes
NGC1398	03h38m52.13s	−26d20m16.2s	1396	19.78	$27.70 \pm 0.53$	$9.41 \pm 0.07$	$11.01 \pm 0.05$	0.47	Yes
NGC2217	06h21m39.78s	−27d14m01.5s	1619	21.87	$37.50 \pm 0.80$	$9.63 \pm 0.06$	$10.79 \pm 0.07$	0.05	Yes
NGC7020	21h11m20.09s	−64d01m31.2s	3201	29.40	$4.96 \pm 0.29$	$9.01 \pm 0.14$	$10.48 \pm 0.07$	0.24	No
NGC1291	03h17m18.59s	−41d06m29.0s	839	4.40	$91.60 \pm 1.09$	$8.62 \pm 0.03$	$9.89 \pm 0.07$	0.28	Yes
NGC1371	03h35m01.34s	−24d55m59.6s	1463	23.79	$45.50 \pm 1.01$	$9.78 \pm 0.18$	$10.60 \pm 0.09$	0.7	Weak
NSO179-IG013	16h47m20.05s	−57d26m24.6s	842	10.90	$104.00 \pm 1.44$	$9.46 \pm 0.09$	$9.77 \pm 0.04$	0.11	No
NGC1079	02h43m44.34s	−29d00m12.1s	1452	25.20	$18.60 \pm 0.63$	$9.45 \pm 0.08$	$10.44 \pm 0.07$	0.12	Weak
NGC5101	13h21m46.24s	−27d25m49.9s	1868	17.23	$20.00 \pm 0.81$	$9.15 \pm 0.06$	$10.60 \pm 0.12$	0.08	Yes
NC5240	22h41m52.38s	−44d46m01.8s	1765	25.37	$13.20 \pm 0.33$	$9.30 \pm 0.08$	$10.61 \pm 0.04$	0.24	Yes
NGC1350	03h31m08.12s	−33d37m43.1s	1905	18.83	$12.50 \pm 0.31$	$9.02 \pm 0.08$	$10.62 \pm 0.05$	1.07	Yes
NGC2369	07h16m37.73s	−62d20m37.4s	3240	35.30	$17.00 \pm 0.56$	$9.70 \pm 0.13$	$10.62 \pm 0.08$	0.18	No
NGC7098	21h44m16.12s	−75d06m40.8s	2381	29.10	$40.20 \pm 1.15$	$9.90 \pm 0.10$	$11.07 \pm 0.04$	0.22	Weak
NGC1543	04h12m43.25s	−57d44m16.7s	1176	17.19	$11.80 \pm 0.38$	$8.92 \pm 0.07$	$10.60 \pm 0.11$	0.11	Yes
NGC1533	04h09m51.84s	−56d07m06.4s	790	20.20	$65.54 \pm 2.31$	$9.80 \pm 0.08$	$10.54 \pm 0.09$	1.59	Yes
NGC1808	05h07m42.34s	−37d30m47.0s	995	9.29	$89.05 \pm 0.89$	$9.26 \pm 0.05$	$10.16 \pm 0.07$	5.64	No
NGC7531	23h14m48.50s	−43d35m59.8s	1596	22.22	$85.44 \pm 1.63$	$10.00 \pm 0.10$	$10.20 \pm 0.09$	0.18	No
NGC1433	03h42m01.55s	−47d13m19.5s	1076	9.47	$34.60 \pm 0.61$	$8.86 \pm 0.07$	$10.03 \pm 0.05$	0.34	Yes
NGC6300	17h16m59.47s	−62d49m14.0s	1109	12.26	$34.50 \pm 0.52$	$9.09 \pm 0.06$	$10.44 \pm 0.04$	0.13	Yes

bar and those with a weak and/or no bar. The HI mass for our sample galaxies is measured using the relation described in Walter et al. (2008),

$$M_{\text{HI}}[M_{\odot}] = 2.356 \times 10^5 D^2 S_{\text{int}},$$

where  $D$  is the distance in Mpc and  $S_{\text{int}}$  is the ATCA integrated flux in units of  $\text{Jy km s}^{-1}$ . The uncertainties on  $M_{\text{HI}}$  are computed by propagating the errors associated with  $S_{\text{int}}$  as described in Koribalski et al. (2004) and assuming a 10% uncertainty on the distance measures. The HI mass of the sample galaxies is in the range  $8.61 \leq \log(M_{\text{HI}}/M_{\odot}) \leq 10.19$ , with a median HI mass of  $\log(M_{\text{HI}}/M_{\odot}) \sim 9.36$ .

We estimate the stellar mass for our sample using their 2MASS (Skrutskie et al. 2006)  $K_s$ -band magnitudes as described by Equation (3) in Wen et al. (2013). The derived stellar mass for our sample is in the range  $9.77 \leq \log(M_{\star}/M_{\odot}) \leq 11.07$ , with a median value of  $\log(M_{\star}/M_{\odot}) \sim 10.56$ . In Table 2 we list all the relevant derived quantities such as the integrated flux, HI and stellar mass etc, for our sample.

Figure 3(a) shows the HI gas fraction plotted against the stellar mass for the ring galaxy sample ( $f_{\text{HI}} - M_{\star}$  relation). As mentioned, we segregate our ring galaxy sample into two—those

without bars and/or having a weak bar (green stars) and those observed to have a strong bar (orange stars). We compare our ring galaxy sample with the representative xGASS sample (Catinella et al. 2018) (blue points) in order to infer how the HI gas fraction of the ring galaxies relates to their stellar mass. We observe that 11 (~46%) of our sample galaxies appear to be HI-deficient compared to the xGASS sample (i.e., lying below the  $1\sigma$  scatter about the running median of the xGASS sample). In addition, we find that 9 of the 11 (~82%) galaxies identified to be HI-deficient are observed to have a strong bar.

We quantify the degree of HI deficiency of the barred and unbarred galaxies in our sample using the xGASS galaxies as a representative sample. We compute the HI deficiency as follows

$$\text{DEF}_{\text{HI}} = \log(M_{\text{HI,exp}}) - \log(M_{\text{HI,obs}})$$

Where  $\log(M_{\text{HI,exp}})$  is the expected HI mass obtained from the rolling median of the  $M_{\text{HI}} - M_{\star}$  scaling relation for the xGASS sample, and  $\log(M_{\text{HI,obs}})$  is the observed HI mass calculated from our ATCA observations. We also measure the HI deficiency values for the sample by replacing the ATCA-derived HI mass with their HIPASS-derived HI mass. Higher the  $\text{DEF}_{\text{HI}}$  value, more HI-deficient the galaxy and vice-versa. In Table 3 we show



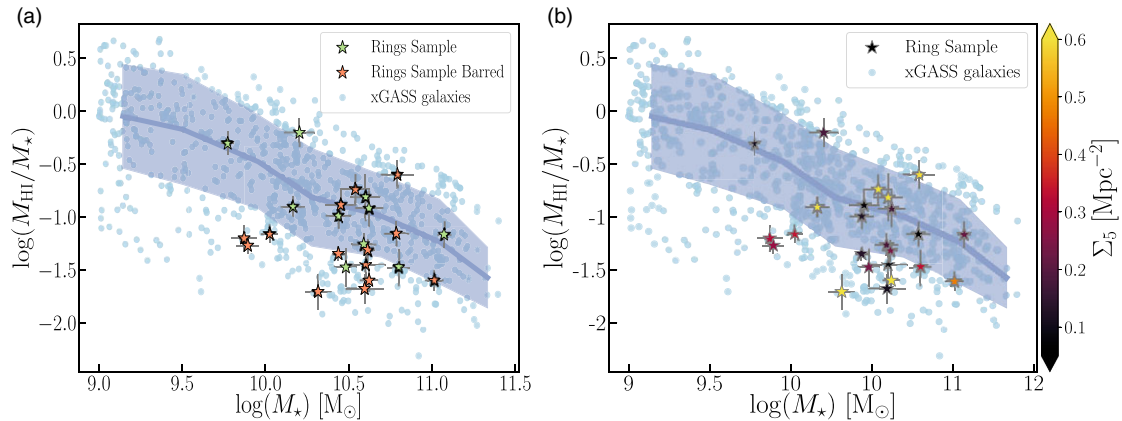


**Figure 3.** (a) The HI gas fraction vs the stellar mass of the ring galaxies compared with the xGASS galaxies (blue points). The green stars represent galaxies in our sample with a weak or no bar and orange stars represent galaxies with a strong bar (b) The  $M_{\text{HI}} - M_*$  relation for the rings sample, this time with the galaxies colour-coded in terms of their  $\Sigma_5$  local environment density values. The dark purple line traces the rolling median of the xGASS galaxies with the shaded region representing the  $1\sigma$  scatter.

the computed median HI deficiency values for both the unbarred and barred galaxies in our sample, and estimate the standard error on the computed median values using a bootstrap re-sampling method. We find that the barred galaxies are significantly more HI-deficient compared to the unbarred galaxies in our sample.

HI deficiency in galaxies has been generally attributed to the effects of the environment. In dense environments, a number of processes tend to strip the HI gas from the discs of galaxies, thereby rendering them HI-deficient. Such processes include, tidal interactions/stripping (Byrd & Valtonen 1990; Rots *et al.* 1990), ram pressure stripping (Gunn & Gott 1972; Chung *et al.* 2009), harassment (Moore *et al.* 1996) among others. To examine if environmental processes are severely affecting the HI gas properties of the observed HI-deficient ring galaxies in our sample, we measure the local environment density for our sample galaxies. We make use of the 5th Nearest-Neighbour projected environment density measure,  $\Sigma_5$  ( $\text{Mpc}^{-2}$ ) (Baldry *et al.* 2006), to probe the local density of the environment the sample galaxies are residing in.

We follow the methods described in Murugesan *et al.* (2020) to estimate the  $\Sigma_5$  values for our sample. The values are estimated based on the 2MASS Redshift Survey (2MRS) catalogue (Huchra *et al.* 2012). With more than  $\sim 43000$  spectroscopic redshift measurements within the magnitude limits,  $K_s \leq 11.75$  mag and  $|b| > 5^\circ$ , the 2MRS catalogue is complete to 97.6% and covers 91% of the entire sky. The below steps are followed to measure the  $\Sigma_5$  values:

- First, we make the 2MRS catalogue volume-limited. We make a velocity cut to the catalogue and include only galaxies with systemic velocities in the range  $200\text{--}8000$   $\text{km s}^{-1}$ . This is then followed by imposing an absolute  $K_s$ -band magnitude cut of  $M_K < -23.45$ , corresponding to the survey's limiting apparent magnitude of 11.75 mag at the highest velocity edge ( $8000$   $\text{km s}^{-1}$ ), thus making the 2MRS sample volume-limited.
- The  $\Sigma_5$  value is computed as  $\Sigma_5 = 5/\pi D^2$ , where  $D$  is the projected distance in Mpc to the 5th nearest-neighbour within  $\pm 500$   $\text{km s}^{-1}$  of the target galaxy.

Figure 3(b) shows the  $f_{\text{HI}} - M_*$  relation for the ring sample, but now the galaxies are colour-coded based on their  $\Sigma_5$  values.

We find that overall, the majority of our sample galaxies are from lower-density environments such as the field and/or loose groups. However, few galaxies in our sample are from high-density environments such as dense groups and cluster. Based on the  $\Sigma_5$  values and the HI and optical morphology of the galaxies in our sample, we do not find any significant evidence that the HI deficiency is driven by environmental effects. This is suggestive that other internal processes may be driving their HI deficiency. As mentioned earlier, since  $\sim 82\%$  of the HI-deficient galaxies in our sample possess a strong bar, it may be the case that the bar is playing an important role in driving the HI deficiency among the barred galaxies in our sample.

The bar has been proposed to play a vital role in the evolution of galaxies, specifically in the context of angular momentum (AM) transport and redistribution of matter within the galactic disc (Sorensen, Matsuda, & Fujimoto 1976; Athanassoula & Bosma 1985; Knapen 2005b). Previous simulation studies have shown that the gas in galactic discs experience torques due to the non-axisymmetric potential of the bar, leading to the dissipation of energy due to collisions in their orbit about the bar, consequently leading to loss in AM and funnelling towards the centre of the galaxy (Bournaud & Combes 2002; Knapen 2005a; Athanassoula 2013). In addition to driving gas to the centre within the co-rotation radius, the bar also effectively transfers AM to the outer parts of the disc, thereby increasing the stability of the HI gas in the outer disc, which remains unavailable for collapse to form stars (Masters *et al.* 2012). This dual effect, that is, funnelling of the gas to the centre inducing star formation and exhaustion of the HI gas (Lin *et al.* 2017), and the transport of AM to the outer disc makes those galaxies having strong bars HI-deficient and redder due to quenching (Masters *et al.* 2012; Newnham *et al.* 2020; Fernandez *et al.* 2021). Our sample galaxies are consistent with these observations, wherein we find that the majority of the strongly barred galaxies are more HI-deficient compared to those galaxies with no bar or weakly barred.

We note that there may be other potential processes driving the HI deficiency in galaxies other than the effects of the bar. This may include interaction-driven tidal perturbations that may lead to starbursts (e.g., Knapen & James 2009; Bergvall *et al.* 2016) and consequent depletion of the HI gas; effects of star formation-driven outflows and the Active Galactic Nuclei (AGN)



**Table 3.** The median HI deficiency values computed for the unbarred and barred galaxies in our sample, using both their ATCA- and HIPASS-derived HI masses. The standard error on the median value is quoted within the brackets.

	DEF <sub>HI</sub> (ATCA)	DEF <sub>HI</sub> (HIPASS)
Unbarred	−0.015 (0.131)	−0.087 (0.106)
Barred	0.455 (0.154)	0.298 (0.174)

in ionising and expelling some fraction of the accreted HI gas out of the disk and into the circumgalactic medium (e.g., Debuhr, Quataert, & Ma 2012; Harrison et al. 2014; Cheung et al. 2016). All of these processes may be contributing to the observed HI deficiency in galaxies. However, as noted earlier in this section, a majority of the galaxies in our sample are from low to intermediate environments and so the effects of tidal interactions is likely to be minimal. In addition, only three galaxies in our sample (NGC 2217, NGC 1808 and NGC 6300) are identified to have any AGN activity. We do note that the current lack of nuclear activity in the majority of the galaxies in our sample does not necessarily mean the AGN was not turned on at an earlier time. This is because AGN activity in galaxies tend to turn on and off at shorter timescales  $\sim 10^5$  yr (Schawinski et al. 2015). Even with this caveat in mind, it is unlikely that AGN-driven winds have played a significant role in driving the HI deficiency among our sample of ring galaxies, mainly because the galaxies in our sample are typically high-mass, that is,  $\log(M_*/M_\odot) \geq 10$ , while AGN-driven HI depletion is generally observed to impact low-mass galaxies, that is,  $\log(M_*/M_\odot) \leq 10$  (see for example Bradford et al. 2018 and references therein). Thus, the majority of our sample is likely not severely affected by AGN-driven HI deficiency. In the next section, we investigate the effects of the bar on the HI gas distribution among our sample galaxies, as well as how the bars may be pivotal in both funnelling HI gas to the centres of galaxies as well as driving resonance rings in the inner and outer parts of the galactic disc.

#### 4. Bar-driven resonance rings

In this section, we study the effects of bars in driving the ring structure among the secularly evolving ring galaxies in our sample. There is a lot of evidence from both observations and models that suggest that bars can lead to the formation of resonance rings (Schwarz 1981; Buta 1986; Buta & Crocker 1991; Sellwood & Wilkinson 1993). The non-axisymmetric gravitational potential of a bar can trigger density waves that leads to orbital resonances where gas and stars can accumulate to form ring-like structures. The location of these orbital resonances (also called Lindblad resonances) depend primarily on the bar patten speed ( $\Omega_{\text{bar}}$ ), the angular velocity ( $\Omega$ ) and the radial epicyclic frequency ( $\kappa$ ) of the gas and stars orbiting the galaxy (Lindblad 1964; Buta 1999). The resonances occur at the radius where the following condition is met:

$$\Omega_{\text{bar}} = \Omega \pm \kappa/m$$

where  $m$  is an integer. The most commonly observed resonances in galaxies are the Outer Lindblad Resonance (OLR), with  $\Omega_{\text{bar}} = \Omega + \kappa/2$ , the Inner Lindblad Resonance (ILR), where  $\Omega_{\text{bar}} = \Omega - \kappa/2$ , the inner Ultra-harmonic Resonance (iUHR)  $\Omega_{\text{bar}} = \Omega - \kappa/4$  and the outer Ultra-harmonic Resonance (oUHR), where  $\Omega_{\text{bar}} = \Omega + \kappa/4$ .

We measure the location of the various resonance radii based on the semi-major axis radius ( $a_{\text{bar}}$ ) and the angular pattern speed of the bar ( $\Omega_{\text{bar}}$ ). Various methods have been proposed in the literature to measure the length of bars in galaxies including visual methods based on where the isophotes diverge from the typical boxy shape of the bar (e.g., Garcia-Barreto & Momjian 2022); bar radius defined as the radius at which the intensity along the major axis of the bar drops to half the intensity of the peak (Salo et al. 2015); as well as based on Fourier analysis (Laurikainen & Salo 2002; Buta et al. 2006).

We measure the bar size visually following the methods described in Garcia-Barreto & Momjian (2022). As the stellar population of the bar is mostly dominated by older stars which are better represented in the IR (see for example Buta 1999; Eskridge et al. 2000; Herrera-Endoqui et al. 2015 and references therein), we make use of the DSS IR-band image to visually determine the radius of the bar ( $a_{\text{bar}}$ ) for our sample of barred ring galaxies. This involves plotting isophotal contours on the DSS IR image and defining the bar radius as the distance from the centre of the galaxy to the last isophote that follows a boxy contour (see Figure 4). We measure the length of the semi-major axis radius of the bar from the centre to each ends of the isophote along the major axis of the bar and take the bar radius to be the average of the two, we term this value  $a_{\text{bar}}^{\text{uncorr}}$ . We compute the standard error on the average value of  $a_{\text{bar}}^{\text{uncorr}}$  and propagate this error when computing the de-projected bar radius  $a_{\text{bar}}$ .

The measured average uncorrected bar radius ( $a_{\text{bar}}^{\text{uncorr}}$ ) is then de-projected to the kinematical major axis of the galaxy, to obtain the corrected bar radius ( $a_{\text{bar}}$ ). Again, this is done following the method described in Garcia-Barreto & Momjian (2022) as:

$$a_{\text{bar}} = a_{\text{bar}}^{\text{uncorr}} \sqrt{\cos^2(\phi) + (\sin^2(\phi)/\sin^2(i))}.$$

Here  $\phi$  is the absolute difference between the median kinematic position angle (P.A) of the disk of the galaxy and the position angle of the bar and  $i$  is the inclination angle of the optical disc of the galaxy as described in Section 2.7.  $a_{\text{bar}}$  is then converted to a physical size in units of kpc using the distance ( $D$ ) to the source. We propagate the errors associated with  $a_{\text{bar}}^{\text{uncorr}}$ ,  $\phi$  and assume a nominal 10% error on the distance measurements to compute the errors on  $a_{\text{bar}}$ . We list the  $a_{\text{bar}}$  values in Table 4.

Once we determine the corrected/de-projected bar radius, we assume the ratio of co-rotation radius of the bar and bar radius,  $R \equiv R_{\text{CR}}/a_{\text{bar}} = 1$ , so that  $R_{\text{CR}} = a_{\text{bar}}$ . A number of previous works have shown that the value of  $R$  ranges from 1 to 1.6 (e.g., Debattista & Sellwood 2000; Guo et al. 2019; Schmidt et al. 2019). While other works have shown that  $\sim 90\%$  of the barred galaxies have  $1.0 \leq R \leq 1.4$  (Athanasoula 1992; Debattista & Sellwood 2000; Starkman et al. 2018). Therefore, setting  $R = 1$  is a reasonable approximation to make for our analysis. Indeed, we find that setting  $R = 1.2$ , which is the average of the range of reported values does not significantly affect our results.

Next, we derive the angular velocity profile ( $\Omega_{\text{HI}}$ ) from the HI gas for our sample galaxies using the HI rotation curve ( $v_{\text{rot}}(r)$ ) extracted from 3DBarolo (see Section 2.7). The observed rotation curve is fit with a simple analytic function introduced in previous works (e.g., Boissier et al. 2003; Obreschkow et al. 2016) and of the form,

$$v_{\text{rot}}(r) = v_{\text{max}} \left(1 - e^{-r/r_{\text{max}}}\right)$$

where  $v_{\text{max}}$  is the maximum rotation velocity corresponding to the flat part of the rotation curve and  $r_{\text{max}}$  is the radius where

**Table 4.** Properties of the bar and Lindblad resonances. Col (1): Common name; Col (2): Average length of the semi-major axis of the bar in kpc; Col (3): Bar pattern speed in units of  $\text{km s}^{-1}\text{kpc}^{-1}$ ; Cols (4)–(7): measured radius of the inner Lindblad resonance (ILR), inner Ultra-harmonic resonance (iUHR), outer Ultra-harmonic resonance (oUHR) and outer Lindblad resonance (OLR) respectively in units of kpc.

Name	$\sigma_{\text{bar}}$ (kpc)	$\Omega_{\text{bar}}$ ( $\text{km s}^{-1}\text{kpc}^{-1}$ )	$R_{\text{ILR}}$ (kpc)	$R_{\text{iUHR}}$ (kpc)	$R_{\text{oUHR}}$ (kpc)	$R_{\text{OLR}}$ (kpc)
(1)	(2)	(3)	(4)	(5)	(6)	(7)
ESO215-31	$10.6 \pm 1.1$	$10 \pm 1$	NA	6.0	22.5	NA
NGC1326	$3.2 \pm 0.3$	$52 \pm 5$	1.91	2.5	4.6	6.8
NGC1398	$5.2 \pm 0.5$	$47 \pm 3$	NA	NA	11.4	21.5
NGC2217	$7.5 \pm 0.8$	$27 \pm 2$	3.4	4.6	13.8	25.1
NGC1371	$3.9 \pm 0.4$	$57 \pm 3$	NA	NA	6.9	11.0
NGC1079	$4.3 \pm 0.4$	$26 \pm 1$	NA	NA	13.0	NA
NGC5101	$6.7 \pm 0.7$	$31 \pm 3$	NA	NA	12.0	NA
IC5240	$3.9 \pm 0.4$	$44 \pm 4$	2.2	3.0	6.0	9.6
NGC1350	$5.3 \pm 0.6$	$39 \pm 4$	NA	3.2	9.2	15.7
NGC7098	$6.1 \pm 0.6$	$47 \pm 10$	4.1	5.1	9.2	14.9
NGC1533	$2.7 \pm 0.3$	$32 \pm 1$	NA	NA	5.8	10.2
NGC6300	$2.2 \pm 0.3$	$90 \pm 13$	NA	NA	2.6	3.6

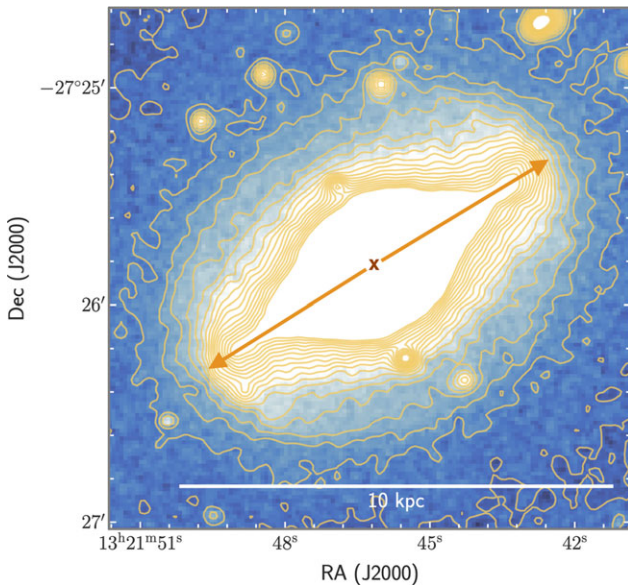


**Figure 4.** DSS IR-band image of the zoomed-in central region of the ring galaxy NGC 5101, showing the bar. The yellow curves are the IR-band isophotal contours overlaid on the image. The red cross denotes the centre of the galaxy and the orange arrows represent the length of bar semi-major axis radius towards each end of the bar along the major axis of the bar.

the rotation curve transitions to the flat part. Both  $v_{\text{max}}$  and  $r_{\text{max}}$  are left as free parameters during the fit. We use the best fitting function describing the rotation curve to then derive the angular velocity profile of the H I gas,  $\Omega_{\text{HI}} = v_{\text{rot}}(r)/r$ , where  $v_{\text{rot}}(r)$  is the circular rotation velocity in  $\text{km s}^{-1}$  and  $r$  is the radius in kpc. We note that the choice of the analytic function used to fit the rotation curves was motivated on the basis of its simplicity as well as the fact that we were able to obtain reasonably good fits for our sample. Following this we measure the bar pattern speed,  $\Omega_{\text{bar}}$ .  $\Omega_{\text{bar}}$  is the angular velocity corresponding to the bar co-rotation

radius  $R_{\text{CR}}$  (see panel (c) in Figure 5). To determine the various Lindblad resonance radii, we first need to derive the epicyclic frequency ( $\kappa$ ), which can be approximated as follows:

$$\kappa(r) = \sqrt{4\Omega_{\text{HI}}^2 + 2r\Omega_{\text{HI}}(d\Omega_{\text{HI}}/dr)}$$

Panel (c) of Figure 5 shows a plot of the angular velocity profile  $\Omega_{\text{HI}}$  as well as the Lindblad curves,  $\Omega_{\text{HI}} - \kappa/2$ ,  $\Omega_{\text{HI}} - \kappa/4$ ,  $\Omega_{\text{HI}} + \kappa/4$  and  $\Omega_{\text{HI}} + \kappa/2$  for the galaxy NGC 7098 (black, blue, green, pink and orange curves respectively). The location of the co-rotation radius ( $R_{\text{CR}}$ ) of the bar is represented by the black dashed vertical line in panel (c) of Figure 5. The bar pattern speed ( $\Omega_{\text{bar}}$ ) is represented by the horizontal black dotted line. The ILR, iUHR, oUHR and OLR radii are determined as the radius at which  $\Omega_{\text{bar}}$  intersects the  $\Omega_{\text{HI}} - \kappa/2$ ,  $\Omega_{\text{HI}} - \kappa/4$ ,  $\Omega_{\text{HI}} + \kappa/4$  and  $\Omega_{\text{HI}} + \kappa/2$  curves respectively. The position angle of the inner rings (ILR and iUHR) is set to be equal to that of the bar position angle, as many previous studies have shown that the inner rings are typically aligned parallel to the major axis of the bar (e.g., Buta & Combes 1996). The position angle of the outer rings (oUHR and OLR) are set equal to the median kinematic P.A. of the galaxy.

Panels (a) and (b) in Figure 5 show the H I moment 0 map and the optical DSS image respectively of NGC 7098 with the ILR, iUHR, oUHR and OLR ring locations indicated by the blue, green, pink and orange ellipses. NGC 7098 is observed to possess an inner ring as well as an outer ring (see DSS optical image in panel (b) of Figure 5) and we find that the predicted location of the oUHR (pink ellipse) coincides nicely with the observed inner ring and the predicted OLR (orange ellipse) traces the outer ring in very good agreement. Additionally, we also observe an H I ring located at the OLR radius.

In addition, we derive the star formation rate (SFR) surface density profiles for our sample to examine if the SFR is enhanced at the locations of the resonance rings. A number of previous works have highlighted that star formation is triggered at the resonance locations in the disc where the H I gas accumulates. We derive the SFR surface density profiles for the galaxies in our sample using

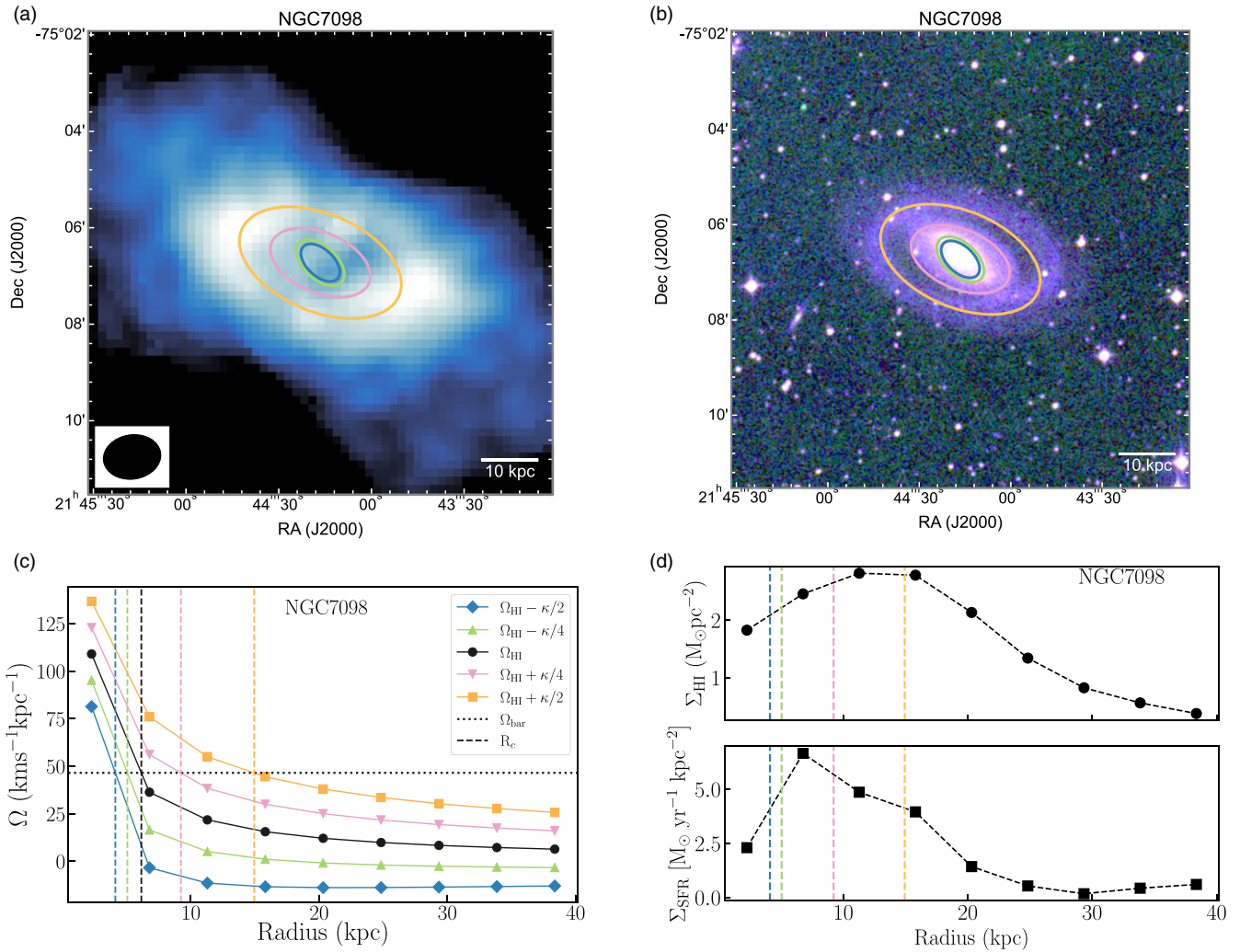


**Figure 5.** (a) HI moment 0 intensity map of NGC 7098. The synthesised beam is shown in the left bottom corner. (b) DSS composite optical image of NGC 7098. The blue, green, pink and orange ellipses represent the location of the ILR, iUHR, oUHR and OLR, respectively. (c) The plot shows the angular velocity ( $\Omega_{HI}$ ; black line) derived from the rotation velocity of the HI gas as a function of radius for the galaxy NGC 7098. The blue, green, pink and orange profiles represent the ILR, iUHR, oUHR and OLR Lindblad resonance curves respectively. The vertical black dashed line represents the measured bar co-rotation radius ( $R_c$ ), the horizontal black dotted line represents the bar pattern speed ( $\Omega_{bar}$ ). The blue, green, pink and orange vertical dashed lines denote the location of the ILR, iUHR, oUHR and OLR resonance radii respectively. (d) Top panel: Radial profile of the HI surface density of the galaxy NGC 7098. Bottom panel: Radial profile of the SFR surface density.

their WISE  $W_3$  and  $W_1$  images procured from the NASA/IPAC IRSA<sup>c</sup> image cutout service. The  $W_3$  flux is shown to be a good tracer of the SFR in galaxies, however, this flux is also contaminated by the contribution from older stellar population (Jarrett et al. 2011; Cluver et al. 2017). We correct for this following the methods described in Cluver et al. (2017) and subtract  $\sim 15.8\%$  of the  $W_1$ -band flux from the  $W_3$  flux.

We first process both the  $W_3$  and  $W_1$  images to remove foreground stars. We run the source finding code SExtractor (Bertin & Arnouts 1996) to identify point-like sources in the images, following this we use the IRAF (Tody 1986) task imedit to replace the bad pixels of the star with random pixels surrounding the star. In the next step we place an annulus around each galaxy and measure the median local sky background values from both the  $W_3$  and  $W_1$

images, before subtracting this from the respective images. Next, we measure both the  $W_3$  and  $W_1$  flux within concentric ellipses, with position angle set to the median kinematic position angle of the galaxy, and convert the corrected  $W_3$  flux to SFR following the methods described in Cluver et al. (2017).

In Panel (d) of Figure 5 we plot both the azimuthally averaged HI surface density ( $\Sigma_{HI}$ ) and the SFR surface density profile ( $\Sigma_{SFR}$ ) for NGC 7098. The inner region ( $<10$  kpc) of this galaxy is observed to have a dip in HI surface density ( $\Sigma_{HI}$ ), while showing a peak in SFR surface density. At the location of the resonance radii, there is an enhancement in  $\Sigma_{HI}$  and  $\Sigma_{SFR}$ . This is also observed in most of the barred galaxies in our sample (see Appendix B for more details) and is consistent with the theory that bars drive resonances, where the disk stars and HI gas accumulate, and the gas eventually collapses to form new stars, thereby resulting in increased SFR at the resonance ring locations (Buta & Combes 1996). Such ring-like structures are likely to remain in equilibrium

<sup>c</sup><https://irsa.ipac.caltech.edu/applications/wise/>.



for a few Gyrs as the resonant locations are regions in the galactic disc where the net torque is zero (e.g., Buta 1999; Bournaud, Combes, & Semelin 2005).

We perform the above resonance model analysis for the rest of the barred galaxies in our sample to see if we are able to predict the location of the resonance rings consistently. We report that there is good agreement between the predicted locations of the resonances and the presence of actual ring-like structures (in HI and/or in the optical) for the majority of the galaxies. We note that depending on the angular velocity profiles, bar radius and pattern speed of the individual galaxies, we are unable to always measure all four resonances. We list the measured bar radius ( $a_{\text{bar}}$ ), pattern speed ( $\Omega_{\text{bar}}$ ) and various resonance radii for the sample in Table 4. Figures B.5–B.9 in Appendix B show the outcomes of the resonance model analysis for the other barred galaxies in our sample.

The measured values of the bar pattern speed ( $\Omega_{\text{bar}}$ ) for our sample range from  $\sim 10$ – $90 \text{ km s}^{-1} \text{ kpc}^{-1}$ , with a median value of  $\sim 44 \text{ km s}^{-1} \text{ kpc}^{-1}$ . This range is consistent with previous works that have measured  $\Omega_{\text{bar}}$  values in galaxies (e.g., Corsini 2011; Williams *et al.* 2021). In addition, we found a few galaxies in our sample for which the  $\Omega_{\text{bar}}$  measurements were available in the literature and find that overall the values are in good agreement. For example, Moore & Gottesman (1995) use VLA HI observations to determine  $\Omega_{\text{bar}}$  of NGC 1398 and estimate a value  $\sim 46 \text{ km s}^{-1} \text{ kpc}^{-1}$ , which is in very good agreement with our measured value of  $47 \pm 3 \text{ km s}^{-1} \text{ kpc}^{-1}$ . Garcia-Barreto *et al.* (1991) measure a pattern speed value of  $\sim 60 \text{ km s}^{-1} \text{ kpc}^{-1}$  for NGC 1326, while we measure a pattern speed of  $52 \pm 5 \text{ km s}^{-1} \text{ kpc}^{-1}$ . We measure  $\Omega_{\text{bar}} 90 \pm 13 \text{ km s}^{-1} \text{ kpc}^{-1}$  for NGC 6300, which is in disagreement with the value measured by Ryder *et al.* (1996), who estimate a bar pattern speed of  $27 \pm 8 \text{ km s}^{-1} \text{ kpc}^{-1}$ . However, we emphasise that the higher  $\Omega_{\text{bar}}$  value we measure predicts the existence of an OLR at a radius of  $\sim 3.57 \text{ kpc}$ , which coincides with the location of both an HI and stellar ring in NGC 6300 (see Figure B.7 in Appendix B). While Ryder *et al.* (1996) report that assuming the lower bar pattern speed of  $\sim 27 \text{ km s}^{-1} \text{ kpc}^{-1}$  would result in the location of an OLR at radius between 8–15 kpc, where they find no HI or stellar ring. The fact that our  $\Omega_{\text{bar}}$  measurement for NGC 6300 better matches the resonance model instils confidence in our analysis.

Overall, from our analysis, we find that the bar driven resonance theory explains the location of the inner and outer rings that we observe among galaxies in our sample. It is indeed promising to note that we are able to reliably measure the location of the various Lindblad resonances using just the HI rotation curve and a visual measurement of the size of the bar. These results come in support of the important role played by the bar in not only funnelling gas to the centres of galaxies but also in driving resonances and redistributing the angular momentum in galactic discs. As noted in Section 3.2, where we observed strongly barred galaxies in our sample to be in general more HI-deficient compared to the weak and non-barred galaxies, it seems evident that bars accelerate the evolution of galaxies via their ability to both use-up large reserves of the HI gas as well as making gas in the outskirts unavailable for star formation due to a kick in angular momentum, thus driving quenching in galaxies.

## 5. Summary and future

We have introduced the new HI in Ring Galaxies Survey (HI-RINGS), comprising of 24 ring galaxies for which we have obtained high-resolution HI observations using the Australia

Telescope Compact Array. The ring galaxies were selected on the basis of their large angular size, their declination range and a detection in the HIPASS catalogue. Our sample consists of a variety of ring galaxies including what have been regarded in the literature as resonance, collisional and interaction rings. We presented an overview of the sample, including their HI, stellar and star formation properties. In addition, we also highlighted their HI morphology and kinematics.

We segregated our sample of ring galaxies into two groups—those with a strong bar and those with a weak or no bar. We find that in general the strongly barred galaxies are more HI-deficient compared to the weakly barred or unbarred galaxies in our sample. We also probed the local environment densities of our sample galaxies in addition to looking at their optical and HI maps to examine if the environment is playing a prominent role in driving the HI deficiency in the galaxies, but find no strong evidence for the same. We therefore hypothesise as suggested by previous works (e.g., Masters *et al.* 2012) that the bars are potentially driving the observed HI deficiency, via their ability to funnel copious amounts of HI gas within the co-rotation radius of the bar to the centres of galaxies. In addition, the bars also transport angular momentum to the outer parts of the disc making the HI gas in the outskirts of galaxies gain a kick in angular momentum and remain stable against collapsing to form stars. This combined effect potentially leads to bar quenching in galaxies as noted in other works.

We also employed Lindblad's resonance theory to test if we are able to predict the radius of the major resonances for a sub-sample of barred galaxies. To determine the resonance radii, we measured the bar radius based on a visual method and combined with the derived rotation curves of the galaxies, we measure the bar pattern speed ( $\Omega_{\text{bar}}$ ) before computing the location of the ILR, iUHR, oUHR and OLR radius. The measured  $\Omega_{\text{bar}}$  values range from  $10$ – $90 \text{ km s}^{-1} \text{ kpc}^{-1}$  in good agreement with previous works. We find that the predicted location of the resonance radii are in good agreement with the observed physical locations of the HI/optical inner and/or outer rings in our galaxies. Furthermore, we derived the azimuthally averaged HI ( $\Sigma_{\text{HI}}$ ) and SFR surface ( $\Sigma_{\text{SFR}}$ ) density profiles for these galaxies and found that there is an enhancement in either  $\Sigma_{\text{HI}}$ ,  $\Sigma_{\text{SFR}}$  or both corresponding to one or more of the resonances.

In forthcoming papers, we aim to study the global and resolved scaling relations for our sample of ring galaxies to see how the different types of ring galaxies behave in the various scaling relations. In addition, we also aim to examine the properties of the collisional and interaction galaxies in our sample. These are interesting systems as the ring structure is believed to be driven by external perturbations. Specifically, as part of the HI-RINGS survey, we have high-resolution HI observations for a recently discovered collisional ring galaxy ESO179-IG013, also called 'Kathryn's Wheel' (Parker *et al.* 2015), which is touted to be the nearest collisional ring galaxy and as such offers a great opportunity to probe its HI and star formation properties. In the near future we aim to address most of the questions posed in the introduction pertaining to the evolution of ring galaxies.

**Acknowledgement.** We would like to thank the anonymous referee for their feedback which significantly improved the quality of the paper. We would also like to extend our thanks to Genevieve Batten, Vaishali Parkash and George Heald for their useful comments and contributions. M.E.C. is a recipient of an Australian Research Council Future Fellowship (project No. FT170100273) funded by the Australian Government. The Australia



Telescope Compact Array is part of the Australia Telescope National Facility (<https://ror.org/05qjv42>) which is funded by the Australian Government for operation as a National Facility managed by CSIRO. We acknowledge the Gomeri people as the traditional owners of the Observatory site. This paper includes archived data obtained through the Australia Telescope Online Archive (<http://atoa.atnf.csiro.au>). This research has made use of the NASA/IPAC Extragalactic Database (NED), which is operated by the Jet Propulsion Laboratory, California Institute of Technology, under contract with the National Aeronautics and Space Administration. This research has made use of the VizieR catalogue access tool, CDS, Strasbourg, France. The original description of the VizieR service was published in *A&AS* 143, 23. This publication makes use of data products from the Two Micron All Sky Survey, which is a joint project of the University of Massachusetts and the Infrared Processing and Analysis Center/California Institute of Technology, funded by the National Aeronautics and Space Administration and the National Science Foundation. This publication makes use of data products from the Wide-field Infrared Survey Explorer, which is a joint project of the University of California, Los Angeles, and the Jet Propulsion Laboratory/California Institute of Technology, funded by the National Aeronautics and Space Administration. Part of this work was performed on the OzSTAR national facility at Swinburne University of Technology. OzSTAR is funded by Swinburne University of Technology and the National Collaborative Research Infrastructure Strategy (NCRIS). This work was written on the collaborative Overleaf platform <https://www.overleaf.com>. This research has made use of python <https://www.python.org> and python packages: `astropy` (Astropy Collaboration et al. 2013, 2018), `matplotlib` (<http://matplotlib.org/> (Hunter 2007)), `APLpy` (<https://aplpy.github.io/>), `pandas` (McKinney 2010), `Jupyter notebook` (<https://github.com/jupyter/notebook>), `NumPy` (<http://www.numpy.org/> (van der Walt, Colbert, & Varoquaux 2011)), `SciPy` (<https://www.scipy.org/> (Jones et al. 2001)) and `CMasher` (<https://github.com/1313e/CMasher> (van der Velden 2020)). This research used Streamlit <https://streamlit.io/>.

**Data Availability.** All data underlying this article is presented in Table 2, Table 4 and the Appendices.

## References

- Appleton, P. N., et al. 1996, *FCPh*, 16, 111
- Astropy Collaboration, et al. 2013, *A&A*, 558, A33
- Astropy Collaboration, et al. 2018, *AJ*, 156, 123
- Athanassoula, E. 1992, *MNRAS*, 259, 345
- Athanassoula, E. 2013, in *Secular Evolution of Galaxies*, ed. J. Falcón-Barroso, & J. H. Knapen (Cambridge University Press), 305
- Athanassoula, E., & Bosma, A. 1985, *ARA&A*, 23, 147
- Bait, O., et al. 2020, *MNRAS*, 492, 1
- Baldry, I. K., et al. 2006, *MNRAS*, 373, 469
- Barnes, D. G., et al. 2001, *MNRAS*, 322, 486
- Bergvall, N., et al. 2016, *A&A*, A72
- Bertin, E., & Arnouts, S. 1996, *A&AS*, 117, 393
- Boissier, S., Prantzos, N., Boselli, A., & Gavazzi, G. 2003, *MNRAS*, 346, 1215
- Bosma, A., van der Hulst, J. M., & Sullivan, W. T., I. 1977, *A&A*, 57, 373
- Bournaud, F., & Combes, F. 2002, *A&A*, 392, 83
- Bournaud, F., Combes, F., & Semelin, B. 2005, *MNRAS*, 364, L18
- Bradford, J. D., Geha, M. C., Greene, J. E., Reines, A. E., & Dickey, C. M. 2018, *ApJ*, 861, 50
- Buta, R. 1986, *ApJSS*, 61, 609
- Buta, R. 1993, *PASP*, 105, 654
- Buta, R. 1995, *ApJSS*, 96, 39
- Buta, R. 1999, *Ap&SS*, 269, 79
- Buta, R. 2001, *VizieR Online Data Catalog*, J/ApJS/96/39
- Buta, R., & Combes, F. 1996, *FCPh*, 17, 95
- Buta, R., & Crocker, D. A. 1991, *AJ*, 102, 1715
- Buta, R., Laurikainen, E., Salo, H., Block, D. L., & Knapen, J. H. 2006, *AJ*, 132, 1859
- Buta, R. J., Byrd, G. G., & Freeman, T. 2004, *AJ*, 127, 1982
- Byrd, G., & Valtonen, M. 1990, *ApJ*, 350, 89
- Catinella, B., et al. 2018, *MNRAS*, 476, 875
- Cheung, E., et al. 2016, *Nature*, 533, 504
- Chung, A., van Gorkom, J. H., Kenney, J. D. P., Crowl, H., & Vollmer, B. 2009, *AJ*, 138, 1741
- Cluver, M. E., et al. 2017, *ApJ*, 850, 68
- Combes, F., Dupraz, C., & Gerin, M. 1990, in *Dynamics and Interactions of Galaxies*, ed. R. Wielen (Berlin, Heidelberg: Springer), 205
- Comerón, S., et al. 2014, *A&A*, 562, A121
- Corsini, E. M. 2011, *MSAIS*, 18, 23
- Dahlem, M., Ehle, M., & Ryder, S. D. 2001, *A&A*, 373, 485
- de Vaucouleurs, G. 1959, *HP*, 53, 311
- de Vaucouleurs, G., et al. 1991, *Third Reference Catalogue of Bright Galaxies. Volume I: Explanations and references. Volume II: Data for galaxies between 0<sup>h</sup> and 12<sup>h</sup>. Volume III: Data for galaxies between 12<sup>h</sup> and 24<sup>h</sup>* (New York: Springer)
- Debbastista, V. P., & Sellwood, J. A. 2000, *ApJ*, 543, 704
- Debuhr, J., Quataert, E., & Ma, C.-P. 2012, *MNRAS*, 420, 2221
- Di Teodoro, E. M., & Fraternali, F. 2015, *MNRAS*, 451, 3021
- Egorov, O. V., & Moiseev, A. V. 2019, *MNRAS*, 486, 4186
- Elagali, A., et al. 2018, *MNRAS*, 481, 2951
- Elmegreen, D. M., Elmegreen, B. G., Combes, F., & Bellin, A. D. 1992, *A&A*, 257, 17
- Eskridge, P. B., et al. 2000, *AJ*, 119, 536
- Fernandez, J., Alonso, S., Mesa, V., Duplancic, F., & Coldwell, G. 2021, *A&A*, 653, A71
- García-Barreto, J. A., Dettmar, R. J., Combes, F., Gerin, M., & Koribalski, B. 1991, *RMxAA*, 22, 197
- García-Barreto, J. A., & Momjian, E. 2022, *AJ*, 164, 91
- Ginsburg, A., et al. 2019, *AJ*, 157, 98
- Grouchy, R. D., Buta, R. J., Salo, H., & Laurikainen, E. 2010, *AJ*, 139, 2465
- Gunn, J. E., & Gott, III, J. R. 1972, *ApJ*, 176, 1
- Guo, R., et al. 2019, *MNRAS*, 482, 1733
- Harrison, C. M., Alexander, D. M., Mullaney, J. R., & Swinbank, A. M. 2014, *MNRAS*, 441, 3306
- Herrera-Endoqui, M., Díaz-García, S., Laurikainen, E., & Salo, H. 2015, *A&A*, 582, A86
- Higdon, J. L., Higdon, S. J. U., & Rand, R. J. 2011, *ApJ*, 739, 97
- Ho, L. C., Li, Z.-Y., Barth, A. J., Seigar, M. S., & Peng, C. Y. 2011, *ApJSS*, 197, 21
- Hoag, A. A. 1950, *AJ*, 55, 170
- Hubble, E. P. 1926, *ApJ*, 64, 321
- Huchra, J. P., et al. 2012, *ApJSS*, 199, 26
- Hunter, J. D. 2007, *CSE*, 9, 90
- Jarrett, T. H., et al. 2011, *ApJ*, 735, 112
- Jones, E., et al. 2001, *SciPy: Open source scientific tools for Python*, [Online; accessed <today>]
- Knapen, J. H. 2005a, *A&G*, 46, 6.28
- Knapen, J. H. 2005b, *Ap&SS*, 295, 85
- Knapen, J. H., & James, P. A. 2009, *ApJ*, 698, 1437
- Knapp, G. R., van Driel, W., Schwarz, U. J., vanWoerden, H., & Gallagher, J. S., I. 1984, *A&A*, 133, 127
- Koribalski, B., Ryder, S., Lopez-Sanchez, A. R., & Karachentsev, I. 2009, *Examining the spiral galaxy NGC7531 and its ghost, ATNF proposal id.C2196*, Semester: October, 2009
- Koribalski, B. S., et al. 2004, *AJ*, 128, 16
- Krumm, N., van Driel, W., & vanWoerden, H. 1985, *A&A*, 144, 202
- Lauberts, A., & Valentijn, E. A. 1989, *The surface photometry catalogue of the ESO-Uppsala galaxies*
- Laurikainen, E., & Salo, H. 2002, *MNRAS*, 37, 1118
- Leroy, A. K., et al. 2008, *AJ*, 136, 2782
- Lin, L., Li, C., He, Y., Xiao, T., & Wang, E. 2017, *ApJ*, 838, 105
- Lindblad, B. 1964, *ApNr*, 9, 103
- Lutz, K. A., et al. 2017, *MNRAS*, 467, 1083
- Lutz, K. A., et al. 2018, *MNRAS*, 476, 3744
- Lynds, R., & Toomre, A. 1976, *ApJ*, 209, 382

- Makarov, D., & Karachentsev, I. 2011, *MNRAS*, **412**, 2498
- Masters, K. L., et al. 2012, *MNRAS*, **424**, 2180
- McKinney, W. 2010, in Proceedings of the 9th Python in Science Conference, ed. S. van derWalt, & J. Millman, 51
- Meurer, G. R., et al. 2006, *ApJSS*, **165**, 307
- Meyer, M. J., et al. 2004, *MNRAS*, **350**, 1195
- Moiseev, A. V., Smirnova, K. I., Smirnova, A. A., & Reshetnikov, V. P. 2011, *MNRAS*, **418**, 244
- Moore, B., Katz, N., Lake, G., Dressler, A., & Oemler, A. 1996, *Natur*, **379**, 613
- Moore, E. M., & Gottesman, S. T. 1995, *ANYAS*, **773**, 329
- Murugesan, C., et al. 2019, *MNRAS*, **483**, 2398
- Murugesan, C., et al. 2020, *MNRAS*, **496**, 2516
- Newnham, L., et al. 2020, *MNRAS*, **492**, 4697
- Nishimura, M., Matsubayashi, K., Murayama, T., & Taniguchi, Y. 2022, *PASP*, **134**, 094105
- Obreschkow, D., et al. 2016, *ApJL*, **824**, L26
- Ochsenbein, F., Bauer, P., & Marcout, J. 2000, *A&AS*, **143**, 23
- Parker, Q. A., et al. 2015, *MNRAS*, **452**, 3759
- Pisano, D. J., Wilcots, E. M., & Liu, C. T. 2002, *ApJSS*, **142**, 161
- Rogstad, D. H., Lockhart, I. A., & Wright, M. C. H. 1974, *ApJ*, **193**, 309
- Rots, A. H., Bosma, A., van der Hulst, J. M., Athanassoula, E., & Crane, P. C. 1990, *AJ*, **100**, 387
- Ryan-Weber, E. V., Webster, R. L., & Staveley-Smith, L. 2003, *MNRAS*, **343**, 1195
- Ryan-Weber, E. V., et al. 2004, *AJ*, **127**, 1431
- Ryder, S. D., et al. 1996, *ApJ*, **460**, 665
- Salak, D., Nakai, N., Hatakeyama, T., & Miyamoto, Y. 2016, *ApJ*, **823**, 68
- Salo, H., et al. 2015, *ApJSS*, **219**, 4
- Sandage, A. 1961, *The Hubble Atlas of Galaxies*
- Sandage, A., & Bedke, J. 1994, *The Carnegie atlas of galaxies*, Vol. 638
- Sault, R. J., Teuben, P. J., & Wright, M. C. H. 1995, in *Astronomical Society of the Pacific Conference Series*, Vol. 77, *Astronomical Data Analysis Software and Systems IV*, ed. R. A. Shaw, H. E. Payne, & J. J. E. Hayes, 433
- Schawinski, K., Koss, M., Berney, S., & Sartori, L. F. 2015, *MNRAS*, **451**, 2517
- Schmidt, E. O., et al. 2019, *AJ*, **158**, 60
- Schneider, S. E., et al. 1983, *ApJL*, **273**, L1
- Schwarz, M. P. 1981, *ApJ*, **247**, 77
- Schweizer, F., et al. 1987, *ApJ*, **320**, 454
- Sellwood, J. A., & Wilkinson, A. 1993, *RPPH*, **56**, 173
- Serra, P., et al. 2015, *MNRAS*, **448**, 1922
- Skrutskie, M. F., et al. 2006, *AJ*, **131**, 1163
- Sorensen, S. A., Matsuda, T., & Fujimoto, M. 1976, *Ap&SS*, **43**, 491
- Starkman, N., Lelli, F., McGaugh, S., & Schombert, J. 2018, *MNRAS*, **480**, 2292
- Theys, J. C., & Spiegel, E. A. 1977, *ApJ*, **212**, 616
- Tilanus, R. P. J., & Allen, R. J. 1993, *A&A*, **274**, 707
- Tody, D. 1986, in *Society of Photo-Optical Instrumentation Engineers (SPIE) Conference Series*, Vol. 627, *Instrumentation in astronomy VI*, ed. D. L. Crawford, 733
- van der Velden, E. 2020, *JOSS*, **5**, 2004
- van derWalt, S., Colbert, S. C., & Varoquaux, G. 2011, *CSE*, **13**, 22
- van Driel, W., & Buta, R. J. 1991, *A&A*, **245**, 7
- van Driel, W., Rots, A. H., & vanWoerden, H. 1988, *A&A*, **204**, 39
- Walter, F., et al. 2008, *AJ*, **136**, 2563
- Wen, X.-Q., et al. 2013, *MNRAS*, **433**, 2946
- Westmeier, T., et al. 2021, *MNRAS*, **506**, 3962
- Williams, T. G., et al. 2021, *AJ*, **161**, 185
- Wilson, W. E., et al. 2011, *MNRAS*, **416**, 832
- Wong, O. I., et al. 2006, *MNRAS*, **370**, 1607
- Wong, O. I., et al. 2017, *MNRAS*, **466**, 574
- Yuan, T., et al. 2020, *NatAs*, [arXiv:2005.11880](https://arxiv.org/abs/2005.11880)
- Zwicky, F. 1941, *Hydrodynamics and the Structure of Stellar Systems*, 137

## Appendix A. Interactive web application to visualise the HI-RINGS sample

Using Streamlit, an open-source Python library for turning data scripts into shareable web applications (<https://docs.streamlit.io/>),

we have built a web application for interactive visualisation of our HI-RINGS survey: <https://hi-rings.streamlitapp.com/>. In [Figure A.1](#) we show a screenshot of the web interface of the application. The application allows the user to interactively explore our sample of ring galaxies using HI intensity data in combination with images from the following surveys: DSS, DSS2 (Blue, Red and Infrared) WISE (3.4, 4.6, 12 and 24  $\mu\text{m}$ ), 2MASS (J, H, K) and GALEX (Far-UV and Near-UV), obtained using the python library astroquery (Ginsburg et al. 2019). There are two options for data display within the web application:

- **Display a survey image and HI contours:** this option is displayed upon opening the application. The user will see (by default) the HI contour at the  $1 \times 10^{20} \text{ cm}^{-2}$  column density level overlaid on top of the galaxy's DSS image, with an image radius of 9 arcmin. The user can then choose another galaxy, and/or adjust the display properties.
- **Compare two images:** this option allows the user to visually compare two personally adjusted images of the selected ring galaxy by dragging the image slider from the centre of the images to the left and right. Image comparison is possible with and without overlaid HI contours, as well as comparison with different survey images in the background. [Figure A.1](#) shows these options (with HI contours), where the left side shows the DSS image while the right side displays the GALEX Far-UV image of the galaxy NGC 1808.

In addition to selecting data display, it is possible to make further adjustments: image radius, display colour options—greyscale or custom colour map and image stretch. Next, the user can adjust the HI contour display options, choosing which density contours they would like to display and which colour map scheme to be used for the contours. We believe such an interactive tool will be both informative as well as provide important visual context into the distribution of the HI and stellar components of the different types of ring galaxies in our sample. By allowing users to personally adjust displays we are extending data visualisation accessibility. Furthermore, a code of this web application is publicly available at: <https://github.com/ringgalaxies/HIRingGalaxies>. *Note: As with any other application, it is highly likely that this application is going to be upgraded with time, and the user interface may differ to the current one shown in [Figure A.1](#).*

## Appendix B. Notes on individual galaxies, 3DBarolo fit parameters and HI spectra

In this section we specify notes on individual galaxies in our sample. As mentioned, the objective of the HI-RINGS survey is to get a complete view of the properties of ring galaxies. Our sample include what appear to be resonance rings as well as collisional rings, ring galaxies with and without a bar. In addition, as mentioned earlier we also comment on galaxies that possess a bar and those that do not and probe the various mechanisms that may be driving their ring-like structure. We note that all morphological classes of the sample galaxies are based on the Carnegie atlas of galaxies (Sandage & Bedke 1994). We also discuss the location of the various Lindblad resonances for the barred galaxies in our sample using the resonance method that was described in [Section 4](#). Additionally, we also note the location of the HI ring, optical ring, spiral arms and show the HI and SFR surface density profiles.

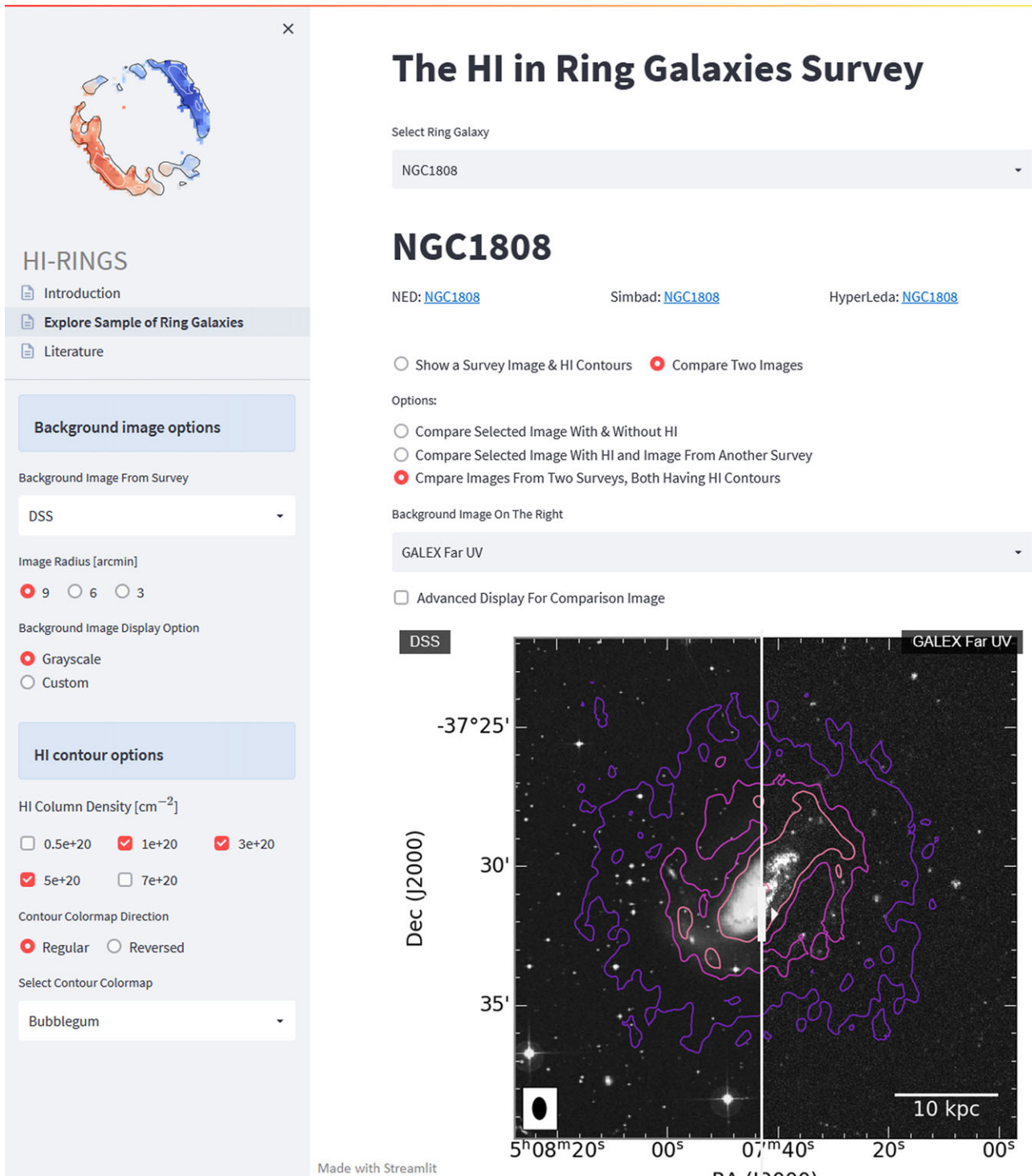


**Figure A.1.** A screenshot showing the user interface of the HI-RINGS Streamlit web application (<https://hi-rings.streamlitapp.com/>) that allows users to visualise our HI-RINGS galaxy sample in a multiwavelength approach. The main available options are: to select a ring galaxy, to show a survey image and HI contours and to compare two images. The user can select a background image from the listed surveys and adjust its display, for example, image radius, colour - greyscale or custom colourmap and image stretch. The user can also adjust the HI contour display options, choosing which HI density contours they want to be displayed and which colourmap to be used for the displayed contours. These options are available for both a single image display and for a comparison of two images from two different surveys.

**Table B.1.** Ring galaxies in our sample categorised into those that are likely to be secularly evolving, those that are identified as collisional/interacting and also segregated on the basis of the presence or absence of bars. Individual notes on interesting systems is also made.

	Secular rings	Collisional/Interaction rings
Barred	<p>Galaxies <b>ESO 215-31, NGC 1302, NGC 1398, ESO 269-57, NGC 1291, NGC 5101, NGC1543, NGC 1350, IC 5240, NGC 1433</b> and <b>NGC 6300</b> are observed to show very similar optical morphologies. We find no strong evidence of interactions or external perturbations of the H I gas for these galaxies and therefore consider these galaxies to be following (semi-)secular evolution. All these galaxies are observed to possess a prominent bar, inner and outer (pseudo-)rings. We note that the H I disc of NGC 6300 is much more extended than its stellar disc unlike the other galaxies in this category, where the H I gas is observed to trace the outer ring and is not much more extended than the ring structure</p> <p>For a subset of the barred galaxies for which we were able to derive accurate rotation curves, bar lengths and bar pattern speeds, we also test the resonance theory to predict the location of the various Lindblad resonances. <b>Figures B.5–B.9</b> show all the relevant plots and images. It is observed that for all galaxies there is a good agreement between the predicted location of the resonances and the presence of ring-like structures either in the optical and/or the H I. In addition, we also show that for most galaxies there is an enhancement in the azimuthally averaged SFR (<math>\Sigma_{\text{SFR}}</math>) and/or H I surface density (<math>\Sigma_{\text{H I}}</math>) profiles corresponding to the radius of the resonances</p>	<p>Galaxies <b>NGC 1326</b> and <b>NGC 2217</b> are observed to have H I tail-like extensions (towards the north for NGC 1326 and towards the north-east and south-west for NGC 2217, respectively, indicating some external perturbation and/or interaction). To what degree the external perturbation has affected the ring formation is uncertain</p> <p><b>NGC 1533</b>—while the optical morphology of this galaxy is observed to be that of an early-type, the H I gas distribution on the other hand is observed to be much more extended and is seen to be linked to two nearby smaller companion galaxies (IC 2038 and IC 2039) to the north-west. Ryan-Weber <i>et al.</i> (2004) note that the amount of extended H I gas in the tail leading to IC 2038/IC 2039 from NCG 1533 is significantly more than what is expected from the size and morphology of IC 2038/IC 2039. Thus, they conclude that the copious amounts of H I gas may have been stripped from a low surface brightness galaxy which is not visible in the optical images. Either way, it is certain that NGC 1533 has recently undergone an interaction and accreted the H I from a low surface brightness galaxy. The H I gas is observed to be distributed in the form of a ring, with no optical counterpart</p>
Unbarred	<p>Galaxies <b>NGC 7020, NGC 2369, NGC 7531</b> and <b>IC 5267</b> are observed to not possess bars. However, from their optical images we find that many of them possess an inner ring and all of them are observed to possess an outer (pseudo-)ring</p> <p>Galaxies <b>NGC 1079, NGC 1371</b> and <b>NGC 7098</b> are observed to have weak bars and outer rings. We note that the H I gas distribution in NGC 1371 is much more extended compared to its stellar disc</p> <p>A Bright linear inclined disc structure is observed in <b>NGC 1808</b>, but not resembling a bar. The H I gas is seen to trace the narrow linear bright central stellar distribution as well as the outer pseudo-ring</p> <p>None of these galaxies show any significant signs of environmental effects as evidenced in their H I kinematic maps. Therefore, we attribute them to be secularly evolving. The origin of their rings therefore is not fully clear</p>	<p><b>NGC 3358</b>—This galaxy has a bright central nucleus and two tightly wound spiral arms extend to form a ring-like outer structure. Corresponding to the outer optical ring is the H I ring of gas. The velocity map of this galaxy shows no obvious deviation from ordered rotational motion. We note that this galaxy is part of an interacting system of at least seven galaxies part of the NGC 3347 group (Makarov &amp; Karachentsev 2011). This galaxy does not appear to possess a bar, therefore the origin of the ring in this galaxy may be attributed to external tidal perturbations</p> <p><b>ESO 179-IG013</b>—This is an interesting candidate as it appears to have undergone an interaction based on both the optical and the H I maps (See upper right panels in <b>Figure B.2</b>) and is described as a collisional ring galaxy by Parker <i>et al.</i> (2015), who term it ‘Kathryn’s Wheel’. In terms of the galaxy morphology ESO 179-IG013 is classified as SB(s)m. The multiwavelength observations of ESO 179-IG013 by Parker <i>et al.</i> (2015) find a ring of star formation based on their H <math>\alpha</math> and optical observations (see <b>Figure 3</b> in their paper). While de Vaucouleurs <i>et al.</i> (1991) classified this galaxy to possess a bar, Parker <i>et al.</i> (2015) argue that this elongated central structure may not actually be a bar but a residual late-type disc. In addition, Parker <i>et al.</i> (2015) identify the system to be the nearest collisional ring to the Milky Way with a systemic velocity of <math>\sim 840 \text{ km s}^{-1}</math>. They also identify the smaller ‘bullet’ galaxy that dropped through ESO 179-IG013, and find its star formation to be enhanced as well. In terms of the H I gas properties, this galaxy is considered the 60th brightest in the sample of 1000 brightest HIPASS galaxies (Koribalski <i>et al.</i> 2004), with an integrated flux of <math>\sim 104 \text{ Jy km s}^{-1}</math>, corresponding to an estimated H I mass of <math>\log(\text{H I}/M_{\odot}) \sim 9.46</math> assuming a distance of 10.9 Mpc. A high-resolution H I follow-up of this galaxy has been lacking until now. As part of the HI-RINGS survey, we present for the first time high-resolution H I follow-up observations for ESO 179-IG013. The H I velocity map of the system shows clear signs of perturbation with H I tails extending towards the south-east and north-west ends of the galaxy</p>

**Figures B.10** and **B.11** display the parameters obtained from the 3D fitting using 3DBarolo as described in **Section 2.7**. Each panel shows the rotation curve, the radial variation of the inclination ( $i$ )

and position angles (PA) for the individual galaxies in our sample. In addition, **Figures B.12** and **B.13** show the extracted ATCA and HIPASS spectra for our sample of ring galaxies.



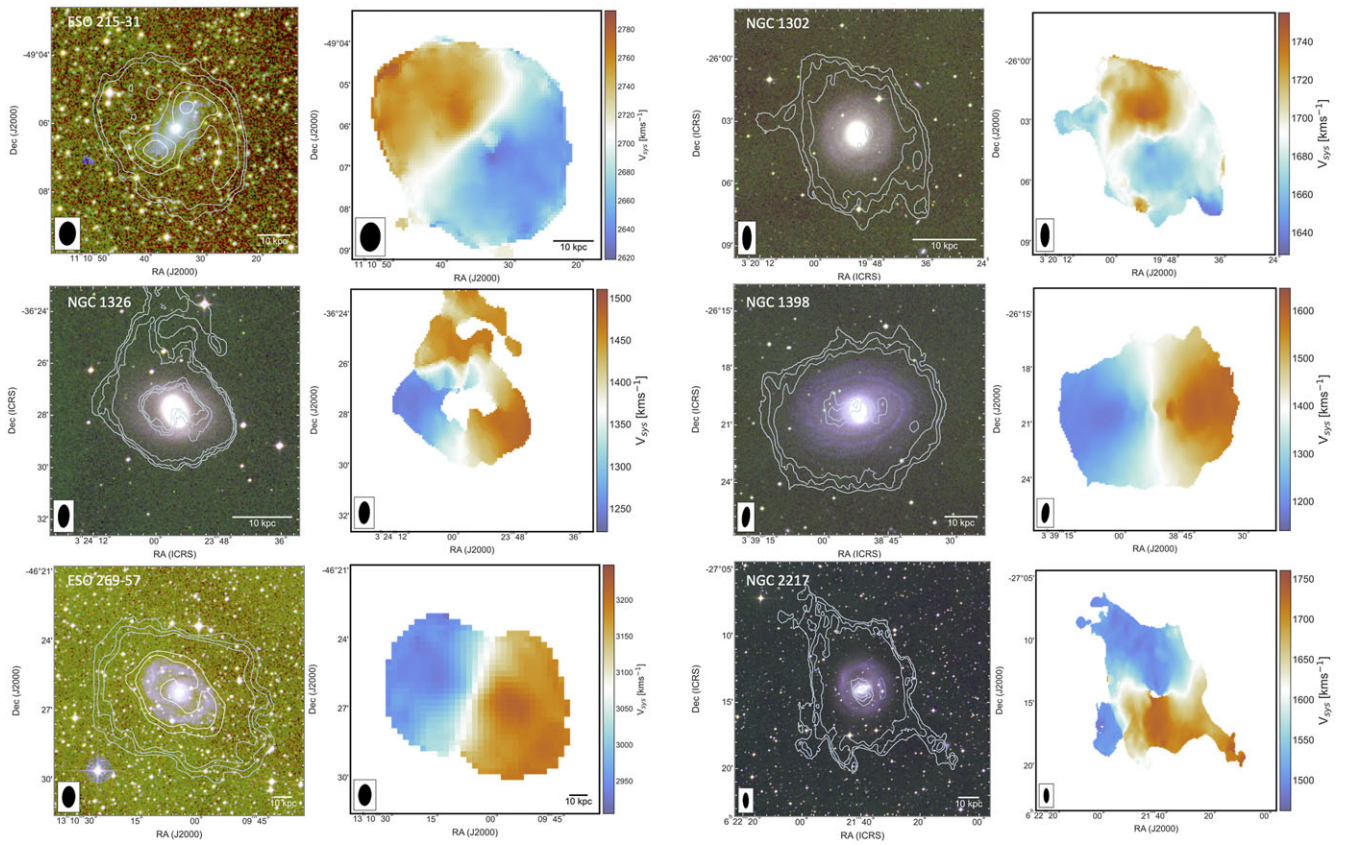


**Figure B.1.** The panels to the left show the HI contours overlaid on top of the composite DSS images of the ring galaxies. The contour levels are at the  $N_{\text{H I}} \sim 0.1, 0.5, 1, 5$  and  $7 \times 10^{20} \text{ cm}^{-2}$ . The panels to the right show the moment 1 (velocity) maps of the HI gas in the rings galaxies. The colour-bars show the velocity range for each individual galaxy.

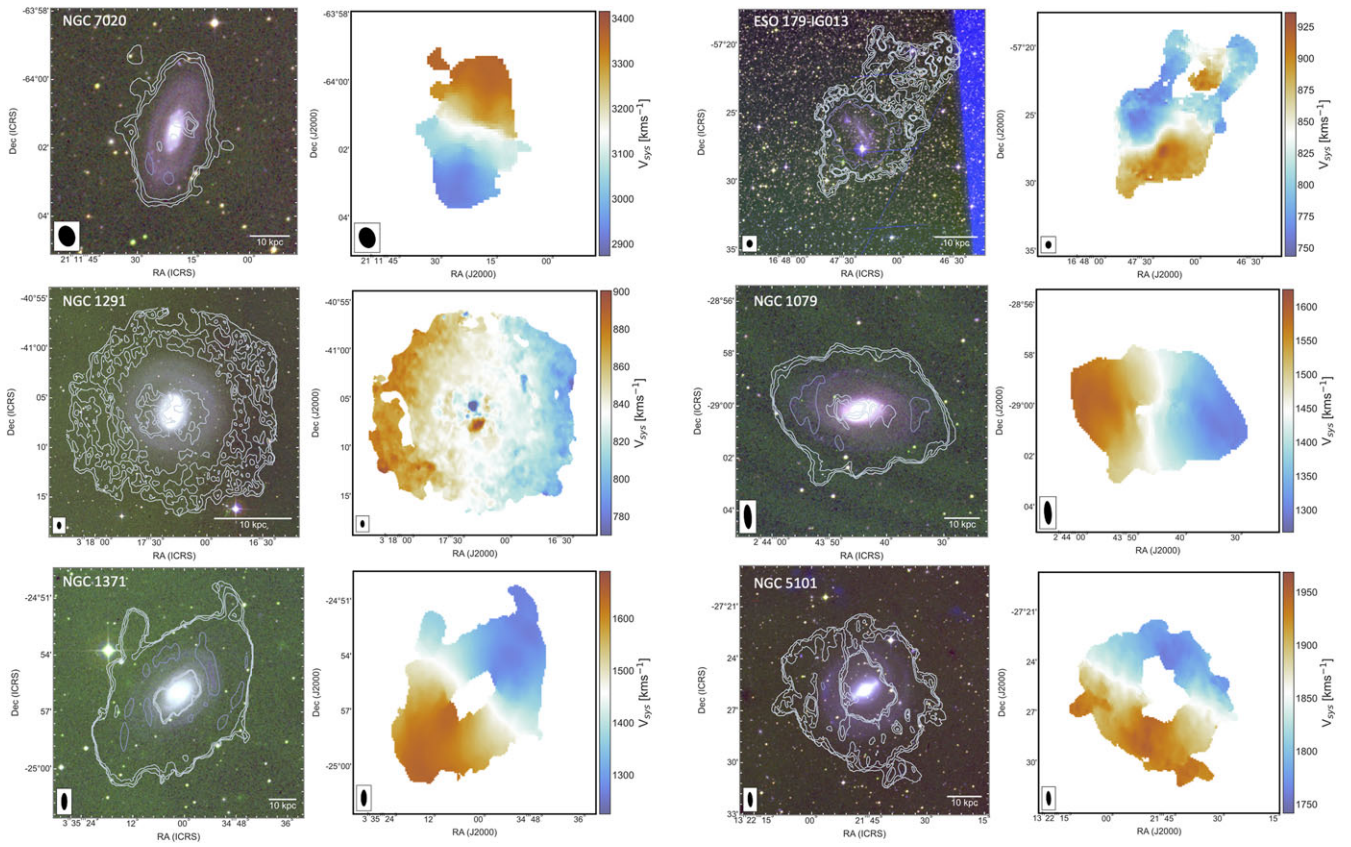


Figure B.2. Same as Figure B.1.

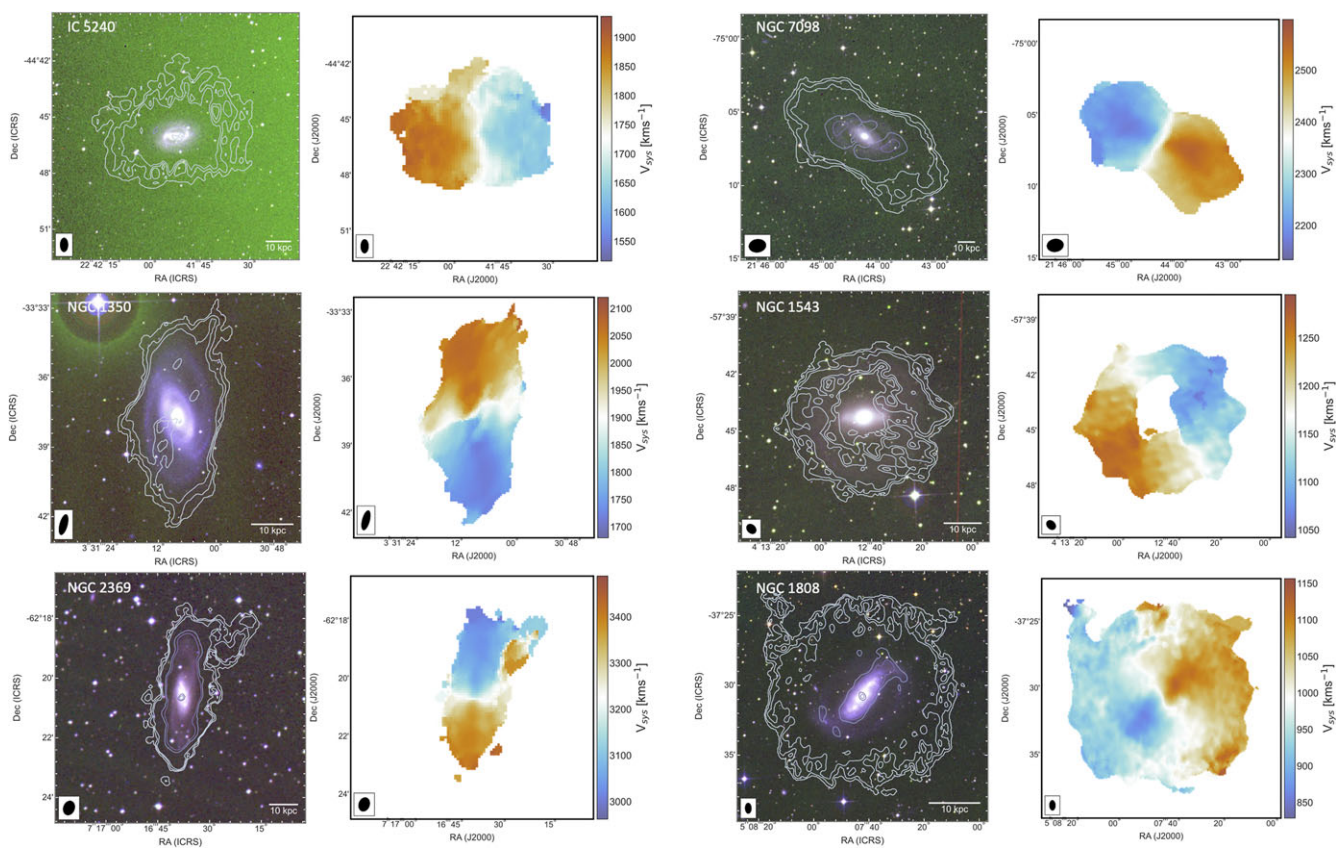


Figure B.3. Same as Figure B.1.



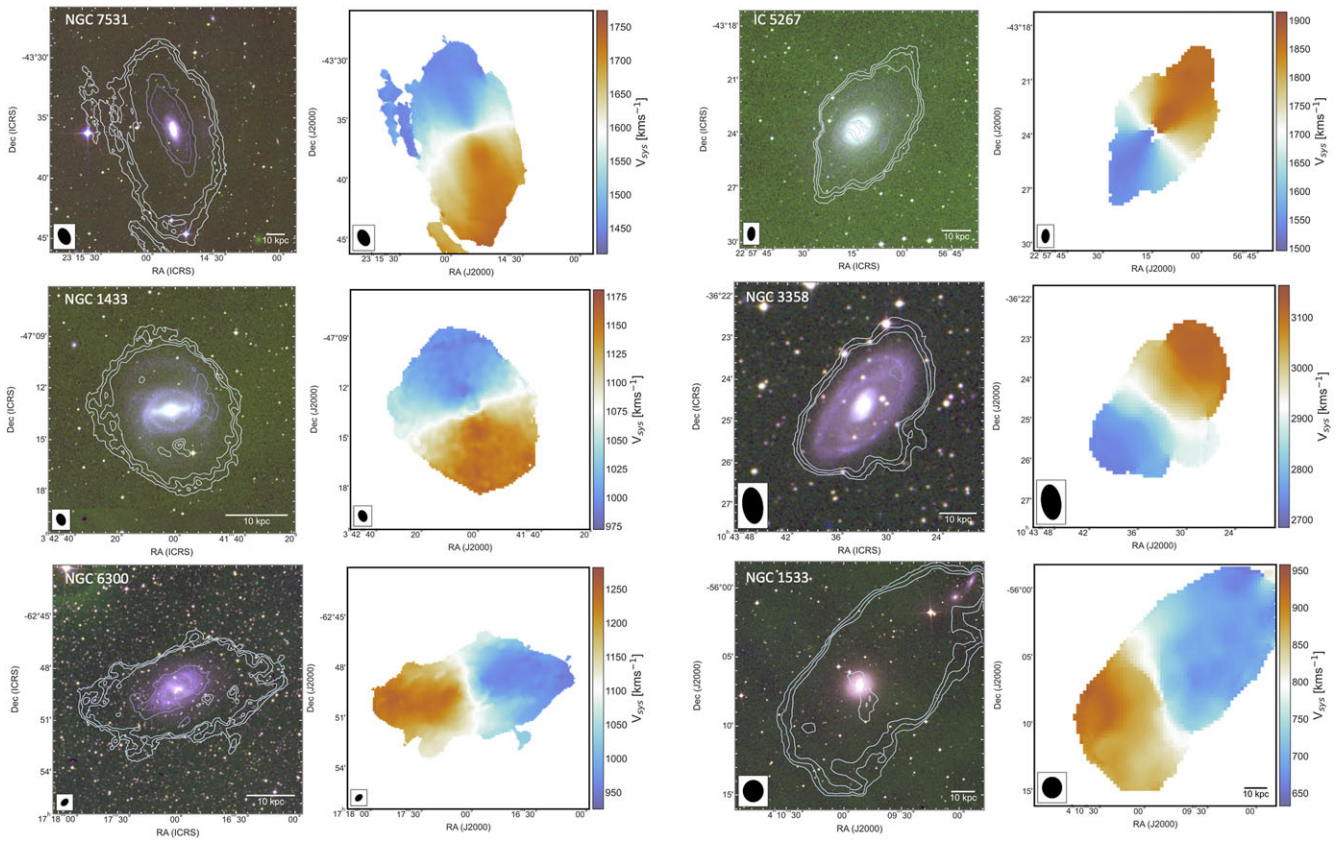
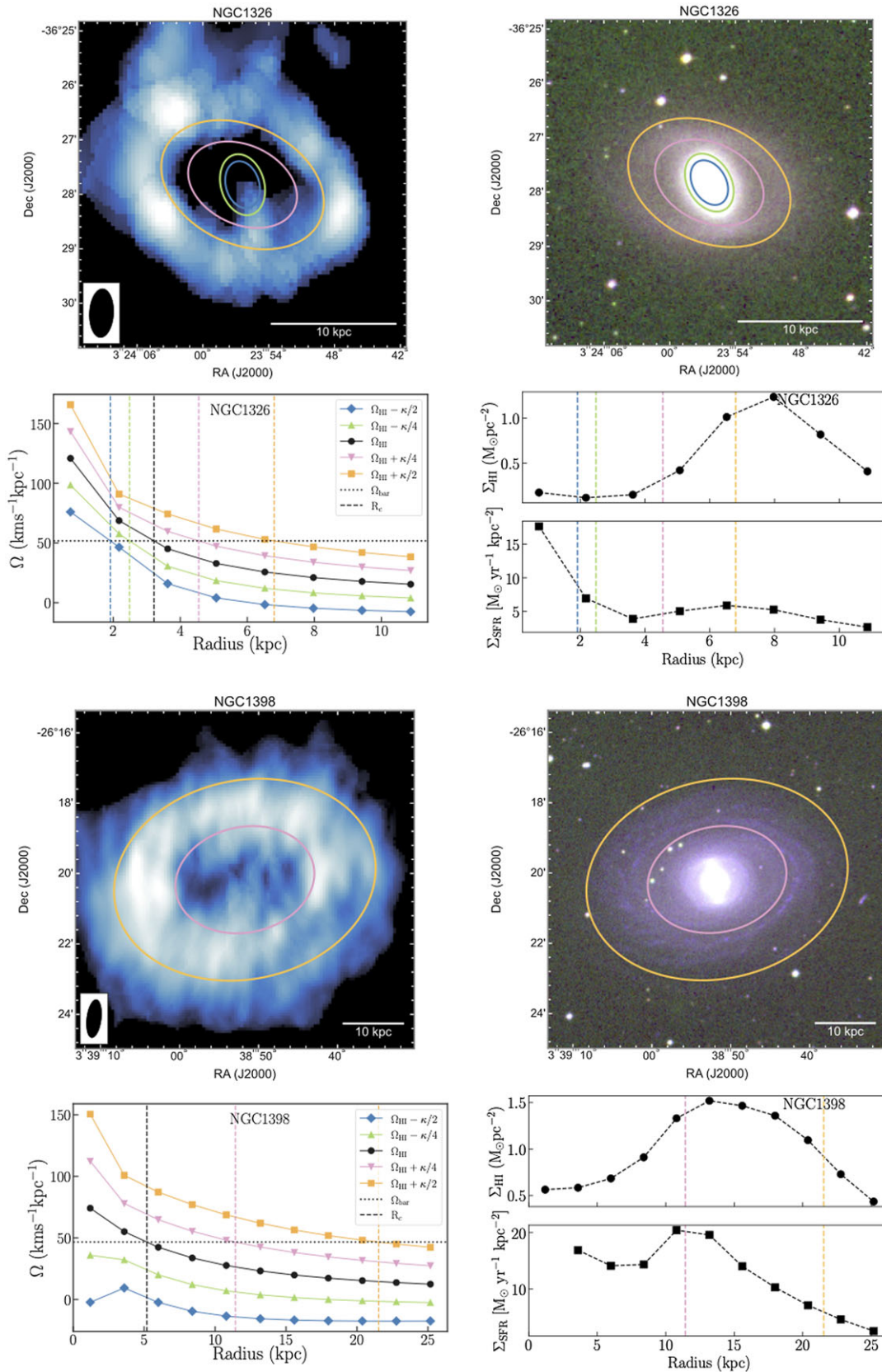
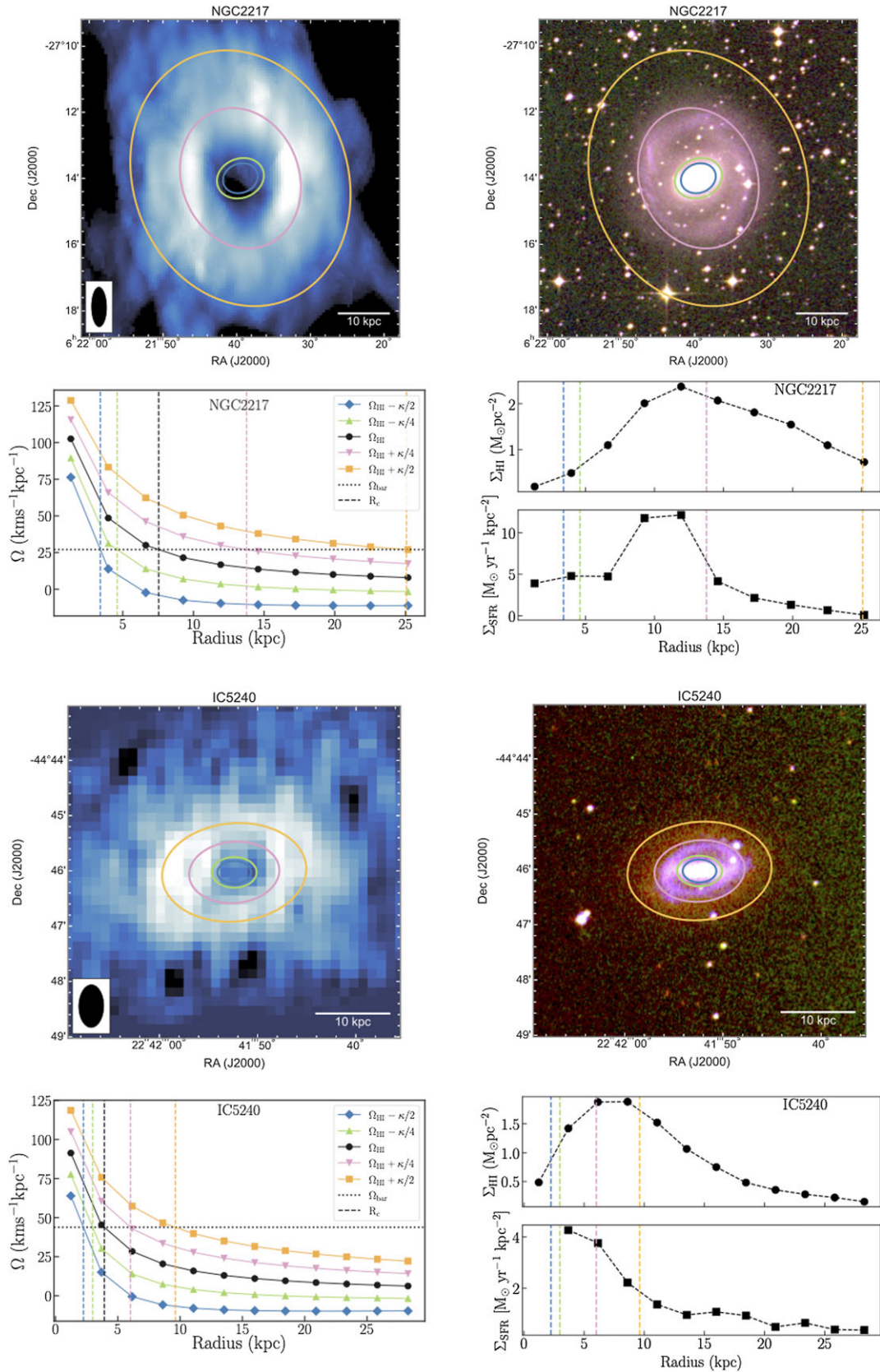


Figure B.4. Same as Figure B.1.





**Figure B.5.** *Top row:* Image to the left shows the moment 0 HI intensity map and image to the right shows the composite DSS image of the galaxy NGC 1326. *Second row:* Left panel shows the angular velocity ( $\Omega_{HI}$ ) profile in black, while the blue, green, pink and orange profiles denote the various Lindblad curves. The radius of co-rotation ( $R_c$ ) is denoted by the black vertical dashed line. The blue, green, pink and orange ellipses (and vertical dashed lines) always represent the ILR, iUHR, oUHR and OLR locations. The bottom two rows are similar to the first two rows but shown for the galaxy NGC 1398.



**Figure B.6.** Top row: Image to the left shows the moment 0 HI intensity map and image to the right shows the composite DSS image of the galaxy NGC 2217. Second row: Left panel shows the angular velocity ( $\Omega_{\text{HI}}$ ) profile in black, while the blue, green, pink and orange profiles denote the various Lindblad curves. The radius of co-rotation ( $R_c$ ) is denoted by the black vertical dashed line. The blue, green, pink and orange ellipses (and vertical dashed lines) always represent the ILR, iUHR, oUHR and OLR locations. The bottom two rows are similar to the first two rows but shown for the galaxy IC 5240.



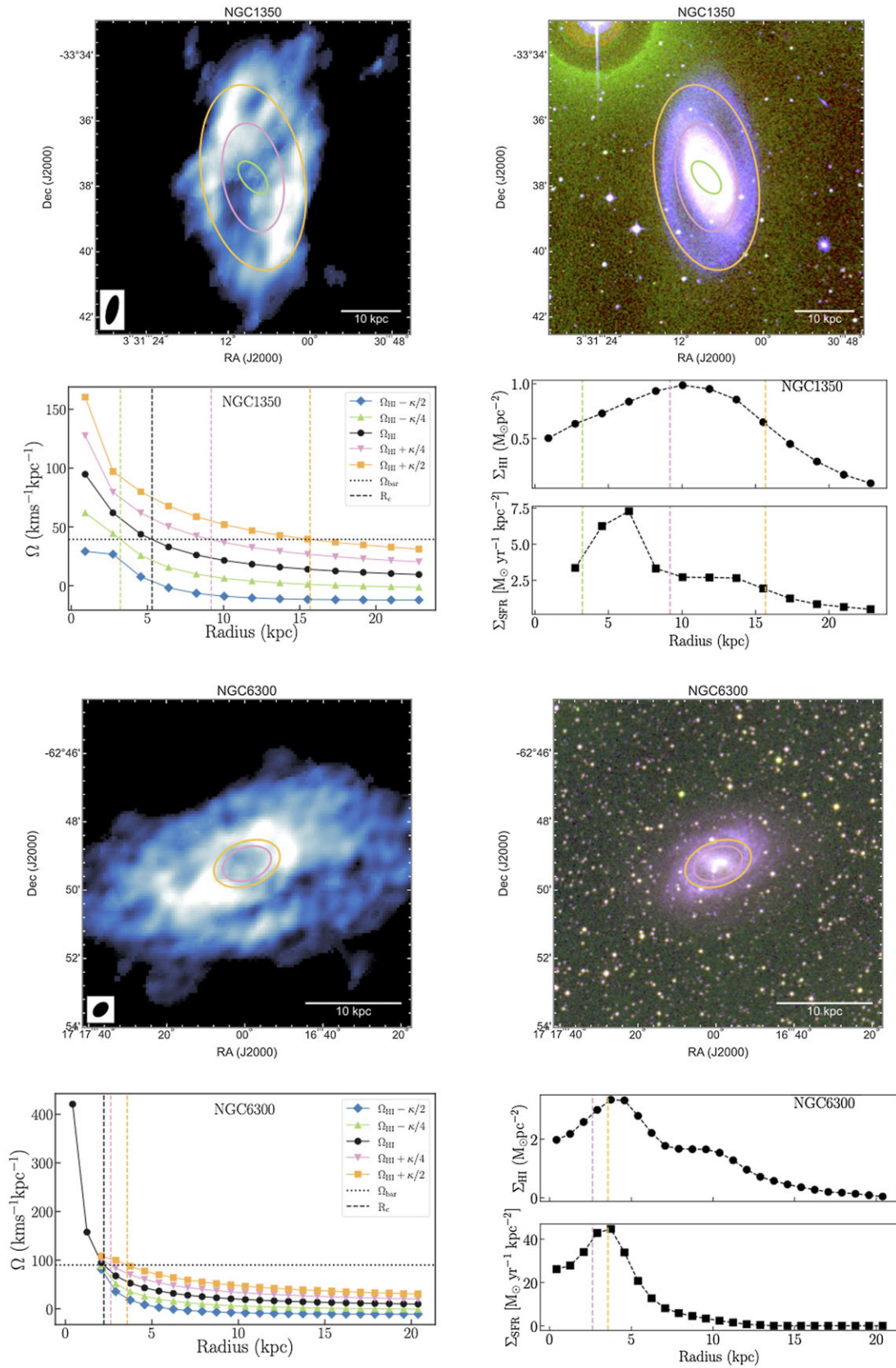


**Figure B.7.** Top row: Image to the left shows the moment 0 HI intensity map and image to the right shows the composite DSS image of the galaxy NGC 1350. Second row: Left panel shows the angular velocity ( $\Omega_{\text{HII}}$ ) profile in black, while the blue, green, pink and orange profiles denote the various Lindblad curves. The radius of co-rotation ( $R_c$ ) is denoted by the black vertical dashed line. The blue, green, pink and orange ellipses (and vertical dashed lines) always represent the ILR, iUHR, oUHR and OLR locations. The bottom two rows are similar to the first two rows but shown for the galaxy NGC 6300.

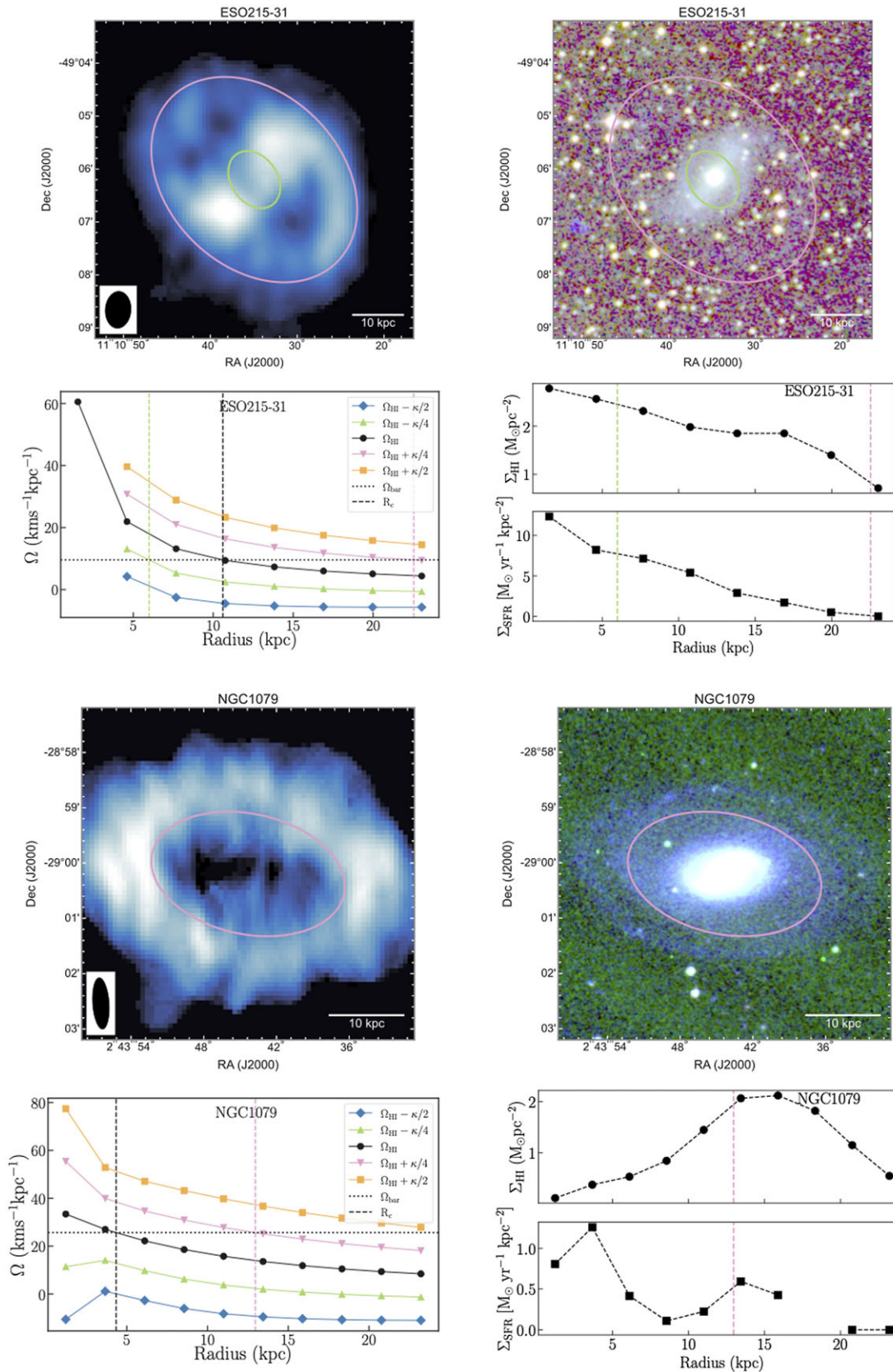


**Figure B.8.** Top row: Image to the left shows the moment 0 H I intensity map and image to the right shows the composite DSS image of the galaxy ESO 215-31. Second row: Left panel shows the angular velocity ( $\Omega_{\text{HI}}$ ) profile in black, while the blue, green, pink and orange profiles denote the various Lindblad curves. The radius of co-rotation ( $R_c$ ) is denoted by the black vertical dashed line. The blue, green, pink and orange ellipses (and vertical dashed lines) always represent the ILR, iUHR, oUHR and OLR locations. The bottom two rows are similar to the first two rows but shown for the galaxy NGC 1079.



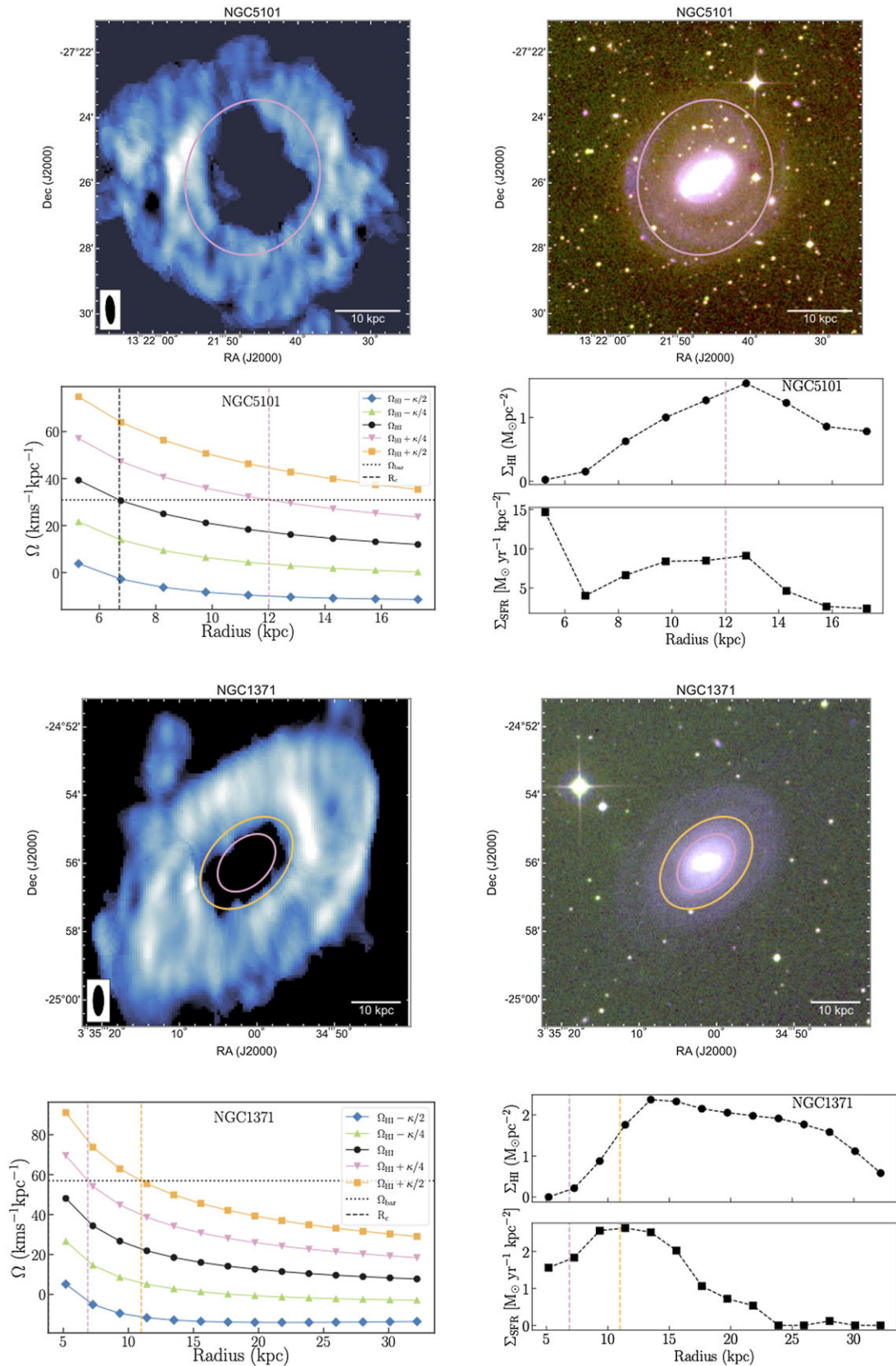


**Figure B.9.** *Top row:* Image to the left shows the moment 0 Hi intensity map and image to the right shows the composite DSS image of the galaxy NGC 5101. *Second row:* Left panel shows the angular velocity ( $\Omega_{HI}$ ) profile in black, while the blue, green, pink and orange profiles denote the various Lindblad curves. The radius of co-rotation ( $R_c$ ) is denoted by the black vertical dashed line. The blue, green, pink and orange ellipses (and vertical dashed lines) always represent the ILR, iUHR, oUHR and OLR locations. The bottom two rows are similar to the first two rows but shown for the galaxy NGC 1371.

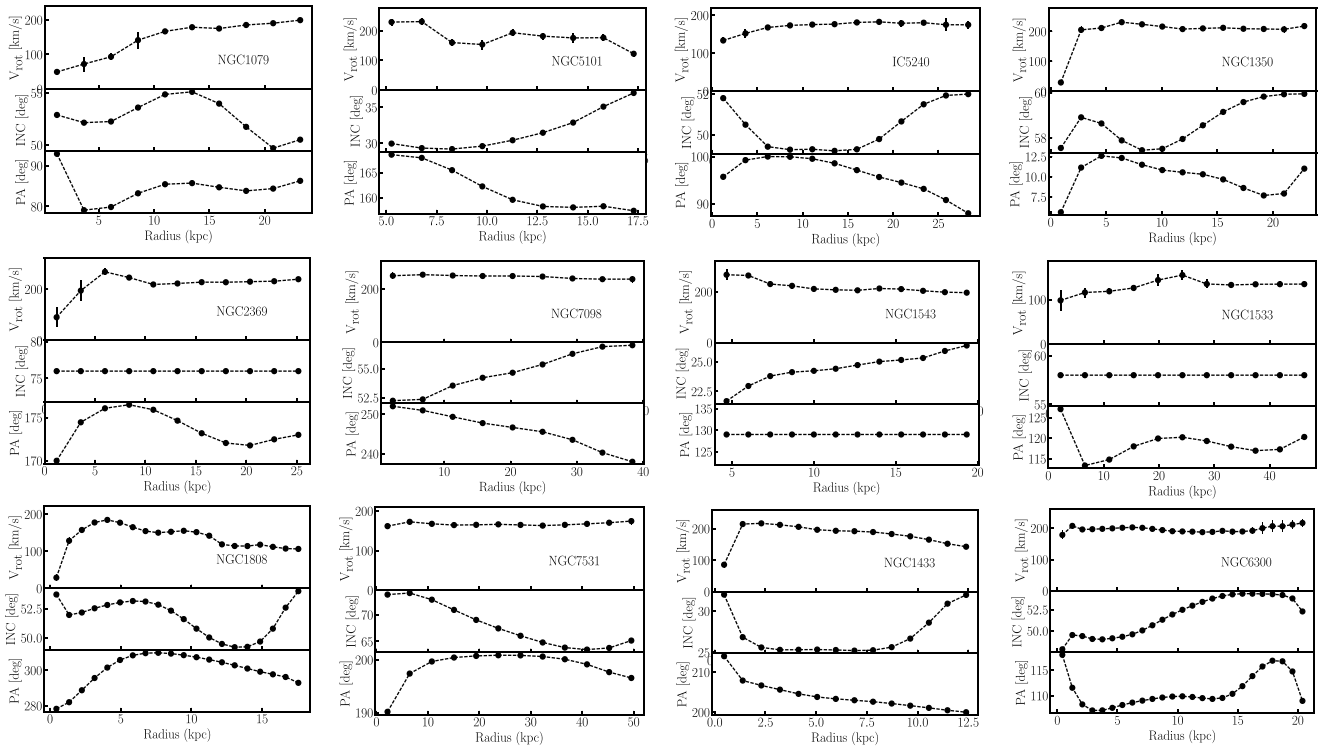


**Figure B.10.** Each panel shows the plots of the rotation curve ( $v_{\text{rot}}$ ) and the radial variation of the inclination ( $i$ ) and position angles (PA) from the 3DBarolo fits to the galaxies.

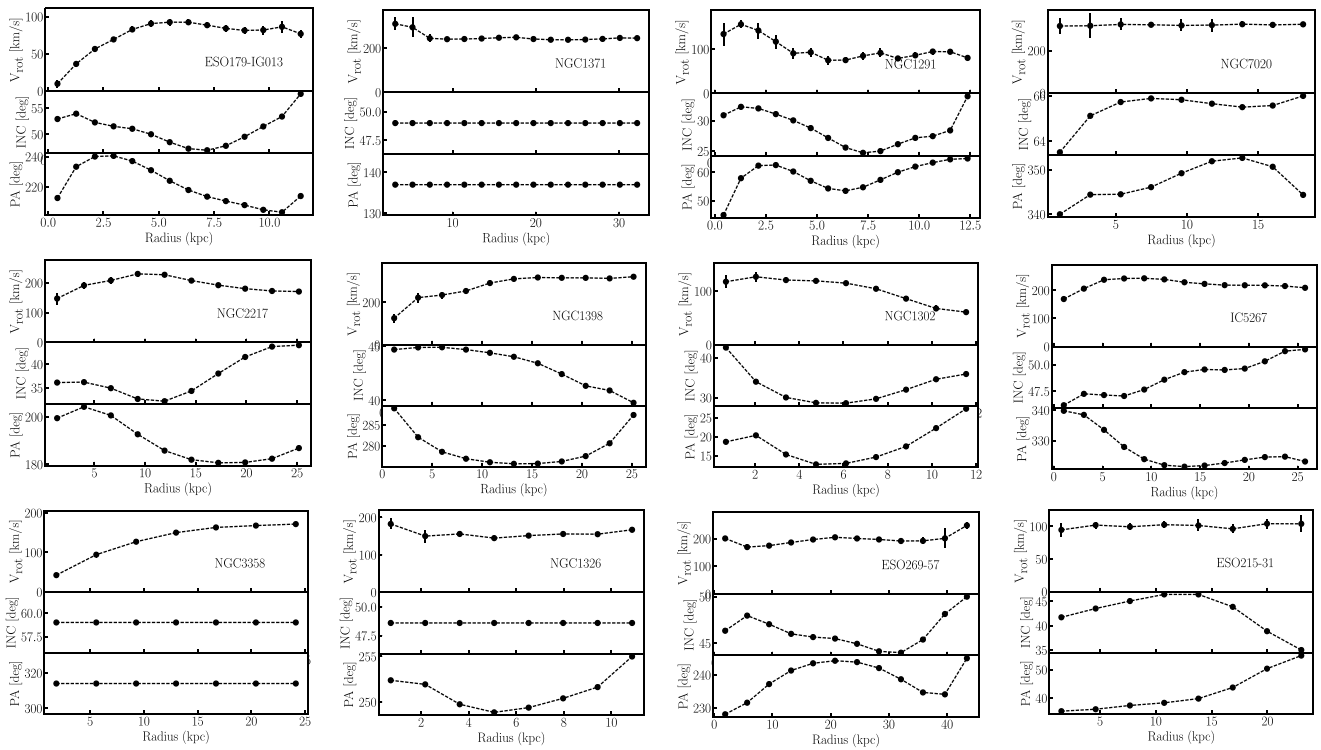


**Figure B.11.** Each panel shows the plots of the rotation curve ( $v_{\text{rot}}$ ) and the radial variation of the inclination ( $i$ ) and position angles (PA) from the 3DBarolo fits to the galaxies.

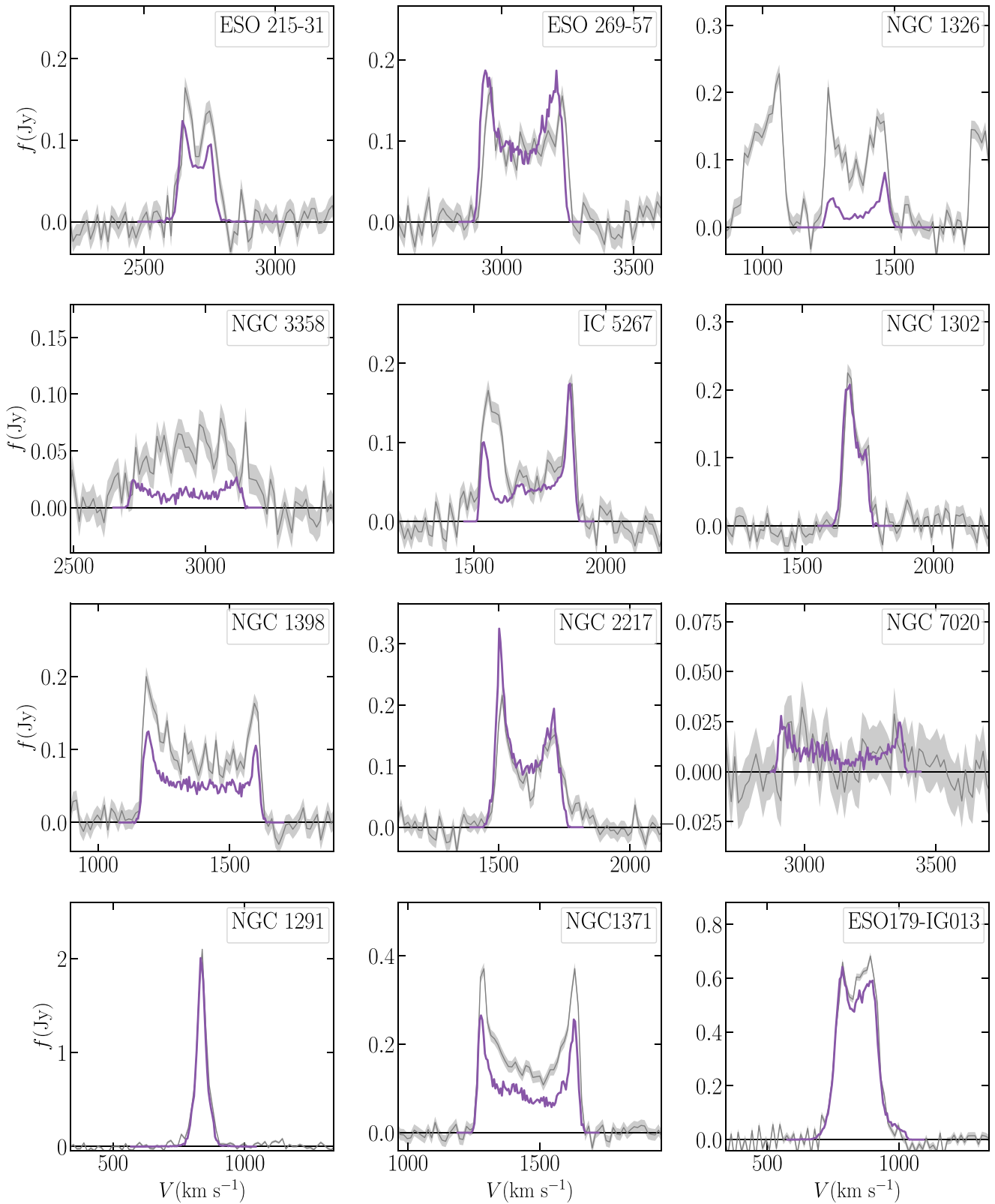


**Figure B.12.** The HI spectra for the HI-RINGS sample. The grey lines are spectra from HIPASS with shaded rms of 13.3mJy and the purple lines are spectra from ATCA observations.

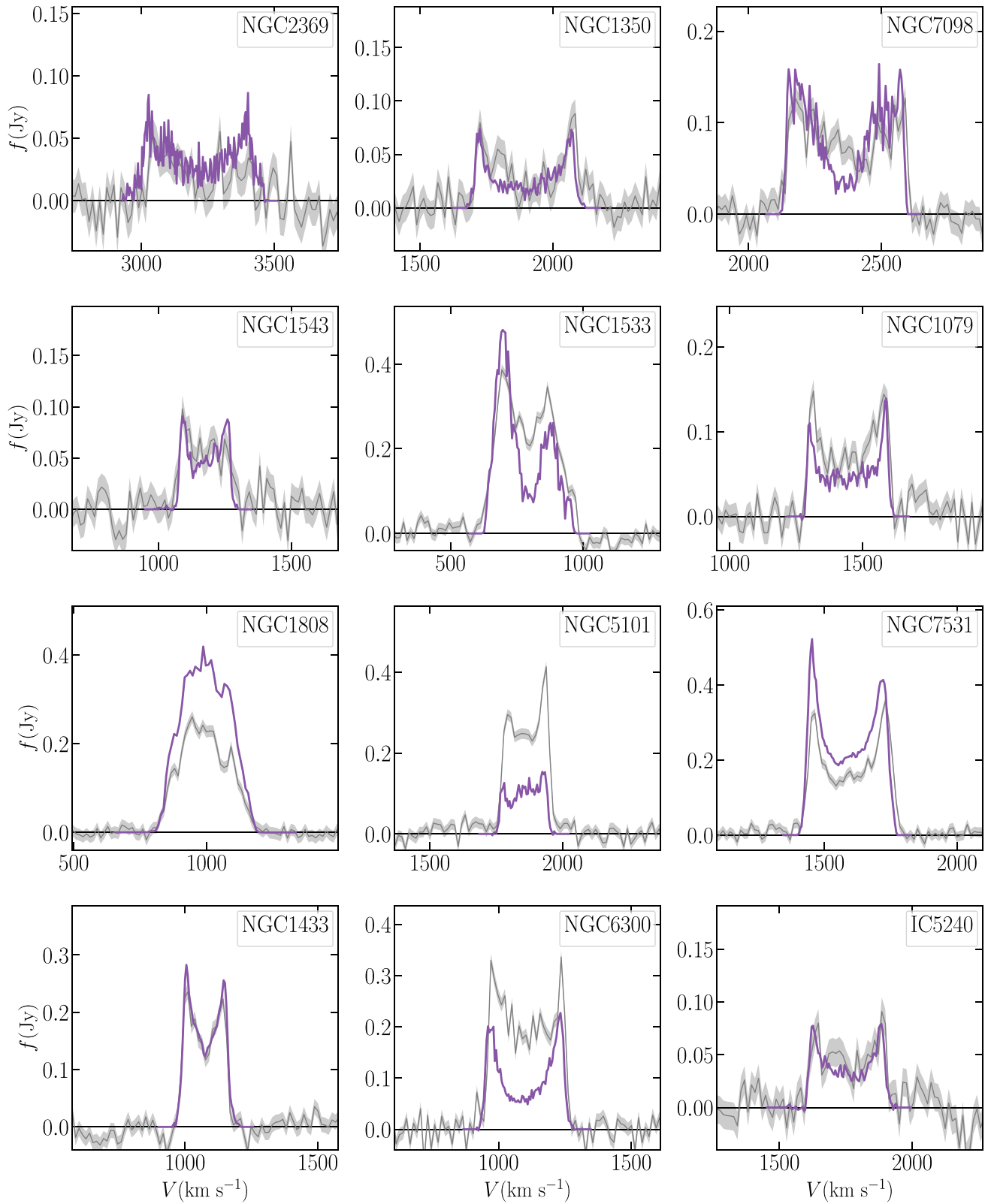


**Figure B.13.** The HI spectra for the HI-RINGS sample. The grey lines are spectra from HIPASS with shaded rms of 13.3 mJy and the purple lines are spectra from ATCA observations.